applied sciences

MDPI

Article

Comparative Study to Evaluate Mixing Efficiency of Very Fine Particles

Sung Je Lee [1] and Se-Yun Hwang [2,*]

[1] TAE SUNG S&E, 27 Seongsui-ro 7-gil, Seongdong-gu, Seoul 04780, Republic of Korea; sjlee@tsne.co.kr
[2] Department of Naval Architecture and Ocean Engineering, Gyeongsang National University, 2 Tongyeonghaean-ro, Tongyeong-si 53064, Gyeongsangnam-do, Republic of Korea
* Correspondence: syhwang@gnu.ac.kr; Tel.: +82-55-772-9196

Abstract

This study evaluates the applicability and accuracy of coarse-grain modeling (CGM) in discrete-element method (DEM)–based simulations, focusing on particle-mixing efficiency in five representative industrial mixers: the tumbling V mixer, ribbon-blade mixer, paddle-blade mixer, vertical-blade mixer, and conical-screw mixer. Although the DEM is widely employed for particulate system simulations, the high computational cost associated with fine particles significantly hinders large-scale applications. CGM addresses these issues by scaling up particle sizes, thereby reducing particle counts and allowing longer simulation timesteps. We utilized the Lacey mixing index (LMI) as a statistical measure to quantitatively assess mixing uniformity across various CGM scaling factors. Based on the results, CGM significantly reduced computational time (by over 90% in certain cases) while preserving acceptable accuracy levels in terms of LMI values. The mixing behaviors remained consistent under various CGM conditions, based on both visually inspected particle distributions and the temporal LMI trends. Although minor deviations occurred in early-stage mixing, these discrepancies diminished with time, with the final LMI errors remaining below 5% in most scenarios. These findings indicate that CGM effectively enhances computational efficiency in DEM simulations without significantly compromising physical accuracy. This research provides practical guidelines for optimizing industrial-scale particle-mixing processes and conducting computationally feasible, scalable, and reliable DEM simulations.

Keywords: discrete-element method (DEM); coarse-grain modeling (CGM); Lacey mixing index (LMI); particle mixing; computational efficiency; powder blending

Academic Editor: Joon Ahn

Received: 7 July 2025
Revised: 2 August 2025
Accepted: 4 August 2025
Published: 6 August 2025

Citation: Lee, S.J.; Hwang, S.-Y. Comparative Study to Evaluate Mixing Efficiency of Very Fine Particles. *Appl. Sci.* **2025**, *15*, 8712. https://doi.org/10.3390/app15158712

Copyright: © 2025 by the authors. Licensee MDPI, Basel, Switzerland. This article is an open access article distributed under the terms and conditions of the Creative Commons Attribution (CC BY) license (https://creativecommons.org/licenses/by/4.0/).

1. Introduction

Particle-mixing processes are widely utilized across various industries, including battery manufacturing [1], chemical processing [2], pharmaceuticals [3], metal components, fertilizers, ceramic materials [4,5], amino acids, and food production [6]. Although the particle types, processing sequences, and methods differ among industries, improvements in mixing efficiency can directly enhance productivity and product quality across applications.

In battery electrode manufacturing, active materials for the anode and cathode are mixed with solvents to form an intermediate slurry. A binder is added to enhance the adhesion between the active material particles, and conductive additives are incorporated

to fill voids between particles, which increases battery capacity. Consequently, the mixing efficiency for the active materials, binders, and conductive additives critically impacts the final product performance.

Similarly, in the pharmaceutical industry, mixing processes are paramount. Over 80% of pharmaceutical products are prepared in solid powder form, which necessitates the blending of various functional powders to achieve the final formulation [3]. Effective mixing ensures sufficient therapeutic efficacy for multifunctional drugs, whereas poor mixing can lead to segregation, thereby degrading clinical performance. Hence, selecting proper mixing equipment and optimizing the operating conditions based on the powder properties is essential. As shown in Figure 1, mixing processes vary significantly across applications, from mechanical vibration and rotational mixing to gas–solid interactions.

Ongoing efforts to optimize mixing processes continue to enhance product quality and reduce manufacturing costs. Historically, mixing was regarded as a secondary step rather than a core production process; hence, limited attention was paid to its economic impact. Consequently, across industries, inefficient mixing was typically addressed by simply prolonging the process instead of optimizing the process parameters. Recently, however, the significance of mixing efficiency has been increasingly recognized, especially as production volumes grow and cycle times shorten. Excessive power consumption from unnecessarily prolonged mixing has emerged as a critical issue that contributes significantly to operational costs. Therefore, evaluating and optimizing mixing efficiency has become increasingly important [7–10].

Mixing efficiency can be assessed experimentally or through numerical simulations. Experimental evaluations usually involve visual observation of particle motion using imaging tools or powder sampling at specific locations. Imaging-based techniques utilize spatiotemporal diagrams to analyze particle movement [11–13] and image processing algorithms for quantitative assessments [14,15]. However, these methods are limited to visually accessible regions, which complicates the evaluation of mixing performance in obstructed zones. Sampling-based approaches [16–18] are more practical but inherently limited since the results depend on the sampling technique, position, quantity, and sample size, even within the same system [19,20]. Even with multiple sampling points, fully capturing both microscopic and macroscopic particle behaviors remains challenging [21].

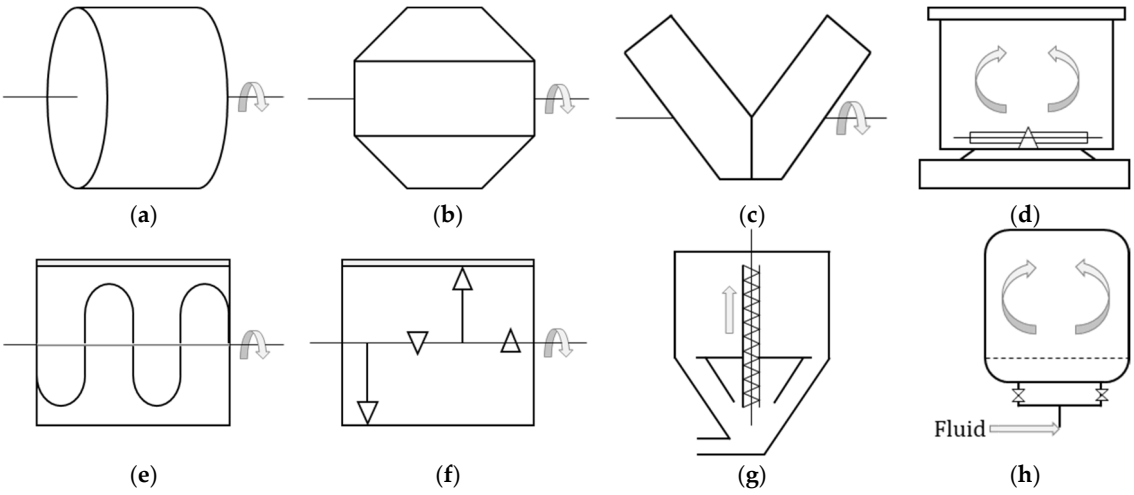

Figure 1. Common industrial mixers for mixing powders and granular materials: (**a**) tumbling-cylinder mixer; (**b**) tumbling-double-cone mixer; (**c**) tumbling V mixer; (**d**) vertical-blade mixer; (**e**) ribbon-blade mixer; (**f**) paddle-blade mixer; (**g**) screw mixer; (**h**) fluidized-bed mixer.

Numerical simulation is generally more cost-effective for complex systems and serves as a foundational tool for scale-up, design, and process control. Computational

methods for mixing simulations include continuum-based and discrete approaches. Continuum models, based on Eulerian–Eulerian frameworks, analyze interactions between particulate flows and surrounding fluids without modeling individual particles explicitly [22]. However, since these models treat particles as a continuous phase, their ability to capture microscopic particle behaviors is limited.

By contrast, discrete methods explicitly track individual particles. Common examples include Monte Carlo methods, cellular automata, and the discrete-element method (DEM). Among these, the DEM is widely used in particle-mixing simulations, such as for drum mixers [23–25], tote blenders [26], and V-blenders [27]. The DEM calculates particle motion at discrete timesteps by solving Newton's second law while accounting for particle–particle and particle–wall interactions. However, it requires significant computational resources; as the particle size decreases, the timesteps must be shortened to maintain contact resolution, which increases the particle count exponentially. These factors significantly increase computational costs, often necessitating high-performance computing resources.

Recent studies highlight the DEM's potential in battery manufacturing optimization. The DEM has been employed to simulate dry mixing in next-generation battery production and evaluate parameters such as viscosity, mixing index, porosity, and stress distribution. These studies emphasize the DEM's utility in understanding microscale interactions and their macroscale implications. Additionally, research on the synthesis of lithium-ion battery cathodes has shown that powder mixing significantly influences electrochemical performance, which underscores the criticality of powder mixing and sets the groundwork for DEM-based modeling [28].

This study verifies the accuracy of DEM simulations incorporating coarse-grain modeling (CGM), which scales up particle sizes to improve computational efficiency. CGM reduces the particle count and allows larger timesteps by increasing the effective particle size, with each scaled-up particle representing a cluster of real particles. We systematically examine five industrial-scale mixing processes via DEM simulations to investigate the impact of varying CGM scaling factors. Mixing efficiency is quantitatively assessed using the Lacey mixing index (LMI), a well-established statistical metric in powder-mixing research.

The contribution of this study lies in identifying the conditions under which CGM delivers reliable results while significantly reducing computational costs. The findings offer valuable guidance for optimizing DEM simulations in mixing applications.

2. Numerical Scheme

Numerical simulations were conducted to investigate various particle-mixing processes and determine whether particle scale-up through CGM introduces significant errors in DEM simulations. Accurate prediction of particle behavior is essential for reliably simulating mixing performance. For this purpose, we utilized the DEM, which tracks individual particle motions at fine time intervals. All simulations were conducted using Ansys Rocky (Release 2024 R2). In DEM simulations, reducing the particle size necessitates proportionally shortening the timesteps to maintain numerical stability. Additionally, maintaining constant mass with smaller particles exponentially increases the particle count, leading to excessive computational demand. CGM addresses this challenge by reducing the particle count and computational cost effectively through particle upscaling. In this study, we specifically evaluated how different CGM scaling factors impact the accuracy of DEM simulations.

2.1. DEM

The DEM is a numerical technique for tracking the motion of a large number of particles. In DEM simulations, particles experience both contact and non-contact forces. Non-contact forces, such as gravity and ambient fluid drag, act continuously, regardless of

collisions, and primarily influence inertial motion. Contact forces, by contrast, arise from collisions and are typically decomposed into normal and tangential components. These forces are calculated iteratively at each timestep and play a critical role in energy dissipation and particle trajectory evolution.

In this study, normal contact forces were modeled using the HLS approach, which accounts for elastoplastic behavior during particle collisions. The HLS model separately defines the loading stiffness during compression and the unloading stiffness during rebound. Plastic deformation is represented by the residual overlap after unloading, while the area between the loading and unloading curves corresponds to the energy loss due to internal friction, heat, or sound. Figure 2 depicts the normal force–overlap relationship, which is mathematically formulated in Equations (1)–(6).

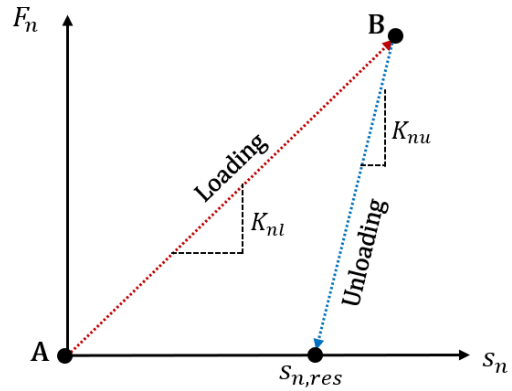

Figure 2. Overlap–normal force relationship in HLS model.

To model tangential contact forces, we employed the LSCL model, which improves upon the basic Coulomb friction model by incorporating sliding stiffness and tangential overlap. The conventional Coulomb model defines tangential forces as simply the product of the friction coefficient (μ) and the normal force (F_n), disregarding contact area deformation and elastic recovery. In contrast, the LSCL model considers tangential stiffness and captures dynamic frictional behaviors more accurately. Figure 3 presents a conceptual definition of overlap and stiffness, and the corresponding force formulations are provided in Equations (7)–(9).

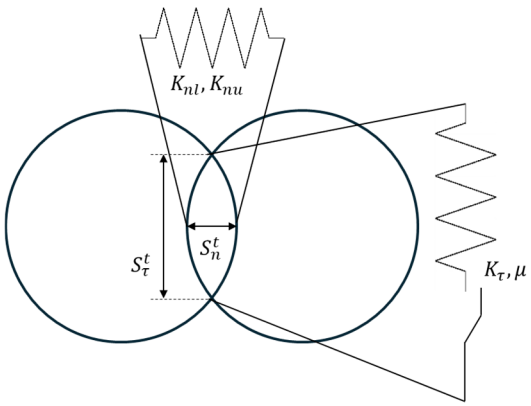

Figure 3. Definition of overlap and stiffness.

The HLS model computes the normal contact force ${F_n}^t$ based on the direction in which the overlap changes. If the normal overlap increases ($\Delta S_n \geq 0$), the force is determined using the loading stiffness F_{nl}, whereas if it decreases ($\Delta S_n < 0$), the unloading stiffness F_{nu} is used with a limiting lower bound defined by a damping parameter γ:

$$F_n^t = min(K_{nl}S_n^t, F_n^{t-\Delta t} + K_{nu}\Delta S_n) \quad if\ \Delta S_n \geq 0, \tag{1}$$

$$F_n^t = max(\ F_n^{t-\Delta t} + K_{nu}\Delta S_n, \gamma K_{nl}S_n^t) \quad if\ \Delta S_n < 0, \tag{2}$$

$$\Delta S_n = S_n^t - S_n^{\Delta t}. \tag{3}$$

Here, F_{nl} and F_{nu} are defined as

$$\frac{1}{K_{nl}} = \frac{1}{K_{nl,p1}} + \frac{1}{K_{nl,p2}}, \tag{4}$$

$$K_{nu} = \frac{K_{nl}}{\varepsilon^2}, \tag{5}$$

$$K_{nl,p} = E_p L, \tag{6}$$

where $K_{nl,p1}$ and $K_{nl,p2}$ represent the stiffness of the particle, L is the particle size, E_p is the bulk Young's modulus, and ε is the restitution coefficient, which represents the energy conservation during a collision.

The LSCL model computes the tangential force F_τ^t as follows: the preliminary elastic tangential force is first calculated using the sliding stiffness K_τ and the change in tangential overlap ΔS_τ; then, this value is limited by the Coulomb threshold μF_τ^t:

$$F_\tau^t = min\left(\left|F_{\tau,e}^t\right|, \mu F_n^t\right), \tag{7}$$

$$F_\tau^t = F_\tau^{t-\Delta t} - K_\tau \Delta S_\tau. \tag{8}$$

The sliding stiffness K_τ is defined in terms of the tangential stiffness ratio r_K and the normal loading stiffness:

$$K_T = r_K K_{nl}. \tag{9}$$

These formulations allow the LSCL model to capture the energy dissipation and dynamic friction in tangential contact scenarios more accurately.

2.2. CGM

CGM enhances the efficiency of DEM simulations by reducing the particle count and lengthening the timesteps through particle-size scaling. CGM aggregates multiple real particles into larger "parcel particles," thus reducing computational requirements significantly without sacrificing simulation accuracy.

The fundamental idea of CGM is to scale up the particle size while preserving the bulk properties. The CGM factor f_{CGM} is defined as the ratio of the parcel particle size to the real particle size:

$$f_{CGM} = L_{parcel}/L_{real}, \tag{10}$$

where L_{real} and L_{parcel} are the diameters of the original particle and the scaled-up particle, respectively. To maintain dynamic similarity, the mass, stiffness, and interaction forces must be adjusted based on the following governing equations:

$$m_{parcel} = {f_{CGM}}^3/m_{real}, \tag{11}$$

$$k_{parcel} = f_{CGM}/k_{real}, \tag{12}$$

$$F_{contact,parcel} = {f_{CGM}}^2/F_{contact,real}, \tag{13}$$

where m is the mass, k is the stiffness, and $F_{contact}$ is the contact force. Figure 4 illustrates the concept of CGM scaling.

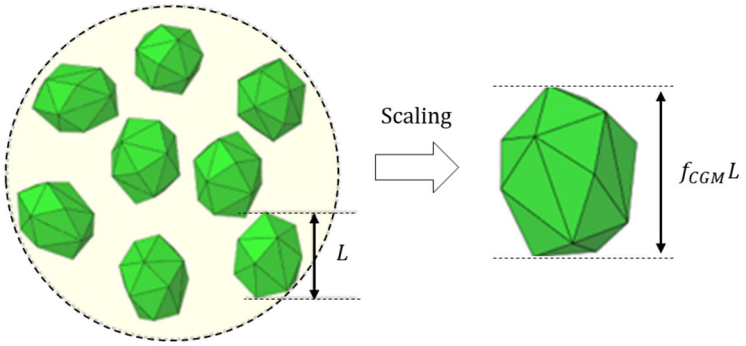

Figure 4. Conceptual representation of CGM.

CGM is especially beneficial for large-scale DEM simulations where direct analysis of real-scale particles is computationally infeasible. Nevertheless, rigorous comparative analysis is necessary to ensure that the deviations introduced by scaling are minimal. We systematically evaluated the applicability and accuracy of CGM across various industrial mixing processes, aiming to identify effective scaling strategies for reliable and computationally efficient simulations.

3. Selection of Mixing Processes

To verify the effectiveness of numerical analyses with coarse-grained particles in DEM simulations, we selected five representative mixing methods, each characterized by distinct operational features. These processes are widely employed across diverse industrial applications.

3.1. Tumbling V Mixer

The tumbling mixer comprises a hollow vessel partially filled with powders or granules that rotate around a horizontal axis, as shown in Figure 5. The material is continuously lifted and dropped during rotation, which promotes thorough mixing and uniform distribution. The rotational speed significantly affects the mixing efficiency; low speeds result in gentle mixing with minimal particle breakage but longer mixing times, whereas higher speeds enhance mixing rates but may cause particle degradation. Excessive speeds could induce centrifugal effects, causing the material to adhere to the container wall and impeding appropriate mixing. Tumbling mixers, including V mixers, are extensively used in the pharmaceutical, chemical, and food industries due to their simplicity and cost-effectiveness. The V mixer selected for this study has a cylindrical chamber with a 600 mm diameter and a 1400 mm height and operates at 10 RPM. We evaluated its mixing efficiency under various CGM scaling conditions.

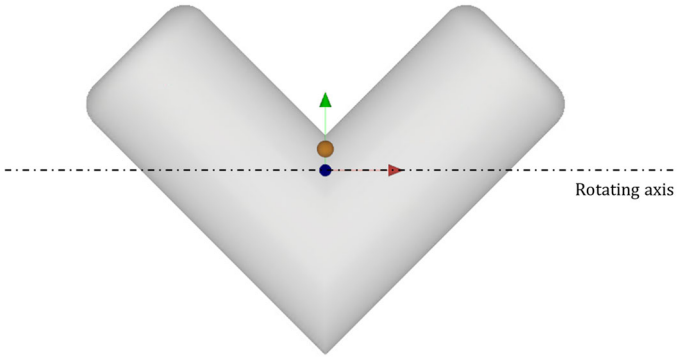

Figure 5. Tumbling V mixer.

3.2. Ribbon-Blade Mixer

The ribbon-blade mixer features a horizontally rotating shaft equipped with helical ribbon blades (Figure 6), which promotes axial and radial movement of the material and ensures comprehensive mixing. The complex flow generated by the interaction between the inner and outer ribbons ensures efficient mixing. The blade geometry considerably influences the mixing efficiency and can be tailored for specific materials. Ribbon-blade mixers are particularly suited for powder-blending applications across the pharmaceutical, chemical, plastic, and agriculture industries. Additionally, they support unit operations, such as heating, cooling, drying, and coating. The ribbon-blade mixer used in this study has a diameter of 1100 mm and a length of 1500 mm, with its blades rotating at 42 RPM.

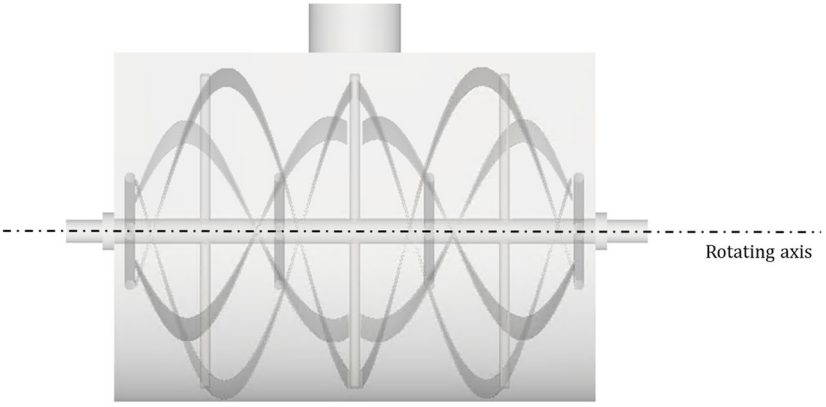

Figure 6. Ribbon-blade mixer.

3.3. Paddle-Blade Mixer

The paddle-blade mixer utilizes a series of rotating paddles to gently lift, fold, and circulate materials, achieving uniform mixing (Figure 7). Unlike ribbon mixers, which are optimized for dry powders, paddle mixers are effective in handling suspensions and mixtures requiring continuous agitation. The paddle configuration can be customized according to the material properties, which enhances mixing efficiency for slurries and high-moisture mixtures requiring gentle handling. The selected paddle-blade mixer measures 960 mm in diameter and 2100 mm in length, with its paddles rotating at 30 RPM.

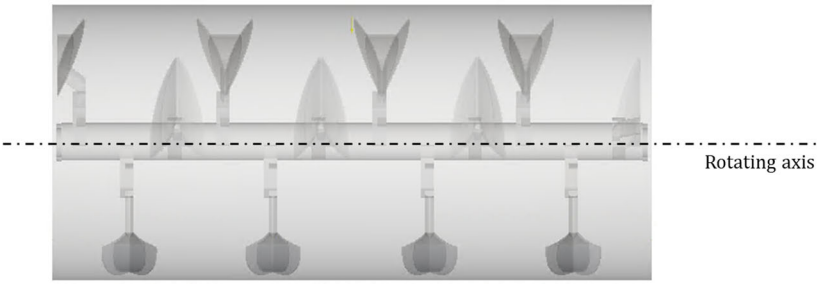

Figure 7. Paddle-blade mixer.

3.4. Vertical-Blade Mixer

Vertical-blade mixers employ high-speed, vertically oriented blades to facilitate efficient blending while consuming less energy than other mixers (Figure 8). Such mixers are particularly effective for high-viscosity materials or simultaneous mixing and particle-size-reduction processes. Their typical applications include mixing cathode active materials with binders in battery manufacturing, as well as processes in the production of chemicals, food, pharmaceuticals, cosmetics, and adhesives. To minimize material adhesion,

such mixers often incorporate a scraper. The selected vertical-blade mixer includes a single vertical blade and a stationary scraper, operating within a 750-mm-diameter container with a height of 430 mm. The container rotates at 15.38 RPM, while the blade rotates at 225 RPM.

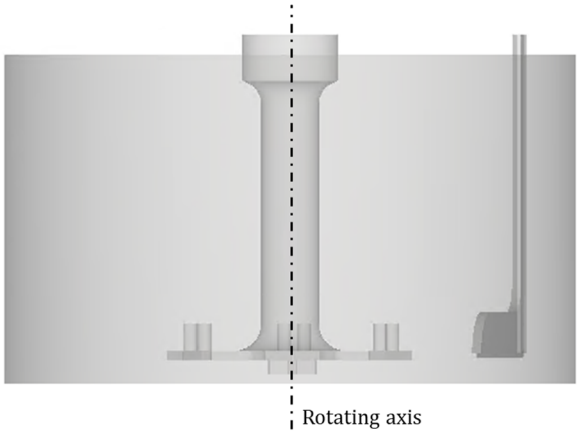

Figure 8. Vertical-blade mixer.

3.5. Conical-Screw Mixer

The conical-screw mixer comprises a stationary conical chamber and a pair of rotating screws that orbit around the vessel's axis, ensuring effective material mixing (Figure 9). This geometry enables complete product discharge, minimizing material residue and thereby reducing product loss. Another advantage is minimal mechanical wear since the internal components rarely contact the material directly. Despite these benefits, such mixers suffer from cleaning difficulties, potential material carryover, and high capital costs due to mechanical complexity. They are widely used in the chemical, petrochemical, pharmaceutical, food, and plastic industries. The conical-screw mixer selected for this study has an upper diameter of 1700 mm, a lower diameter of 500 mm, and a height of 1700 mm. The central arm of the screw assembly orbits at 4 RPM, while each individual screw rotates about its own axis at 57 RPM.

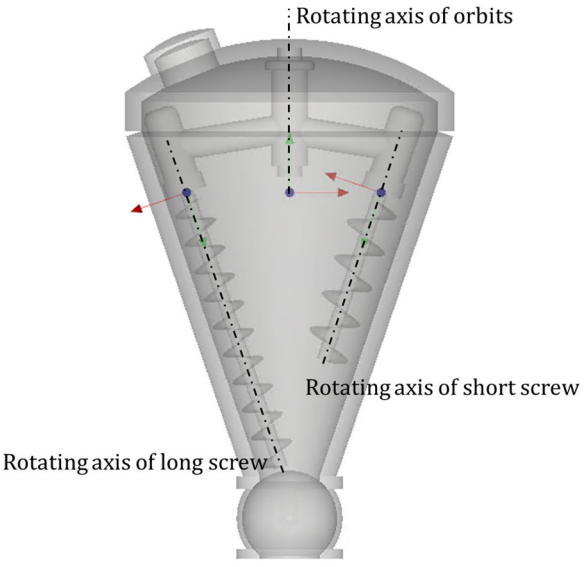

Figure 9. Conical-screw mixer.

4. Numerical Analysis Models

4.1. Particle Modeling

All particles were modeled as spheres to isolate the effects of CGM scaling and to ensure consistency across different mixing-system configurations. Although Ansys Rocky supports non-spherical particle modeling, it incurs a significantly higher computational cost, particularly in high-resolution or large-scale simulations. When the particle size is significantly smaller than the characteristic dimensions of the mixing equipment, such as when the particle diameters are on the order of microns or millimeters while the vessel spans several meters, the influence of the particle shape on the bulk mixing behavior is generally considered negligible. This is particularly true when mixing uniformity is evaluated using statistical indices, such as the LMI. This simplification enabled us to focus on assessing the applicability of CGM and the associated efficiency improvements.

In real-world industrial processes, however, particles often exhibit highly irregular and diverse shapes, which render full geometric representation within DEM simulations computationally prohibitive. Nevertheless, when simulation results are intended for high-fidelity comparison with experimental data or for quantitative validation of specific equipment, incorporating realistic particle shapes may become necessary. In such cases, CGM becomes even more essential as it facilitates the simulation of complex-shaped systems by significantly reducing the particle count and enabling tractable timesteps without severely compromising physical accuracy. Therefore, integrating CGM into the modeling of realistically shaped particles represents a promising direction for future research, particularly studies aiming to bridge simulation and experiment in industrial-scale powder-mixing applications.

To ensure consistency across simulations, we employed a two-particle system in each mixing process. Although real-world industrial scenarios might involve diverse particle types, identical material properties were assigned to all particles in these simulations to avoid variations resulting from differing material properties. Table 1 summarizes the physical properties used for both types of particles in all simulations.

Table 1. Material properties of particles.

Property	Particle 1	Particle 2
Bulk density (kg/m^3)	1900	1050
Bulk Young's modulus (N/m^2)	5×10^7	5×10^7
Friction coefficient	0.2	0.2
Restitution coefficient	0.3	0.3

The sizes and total masses of the particles were adjusted according to the characteristics of each mixing process to maximize computational efficiency. Table 2 summarizes these parameters, while Figure 10 illustrates the initial spatial distributions of the particles before mixing.

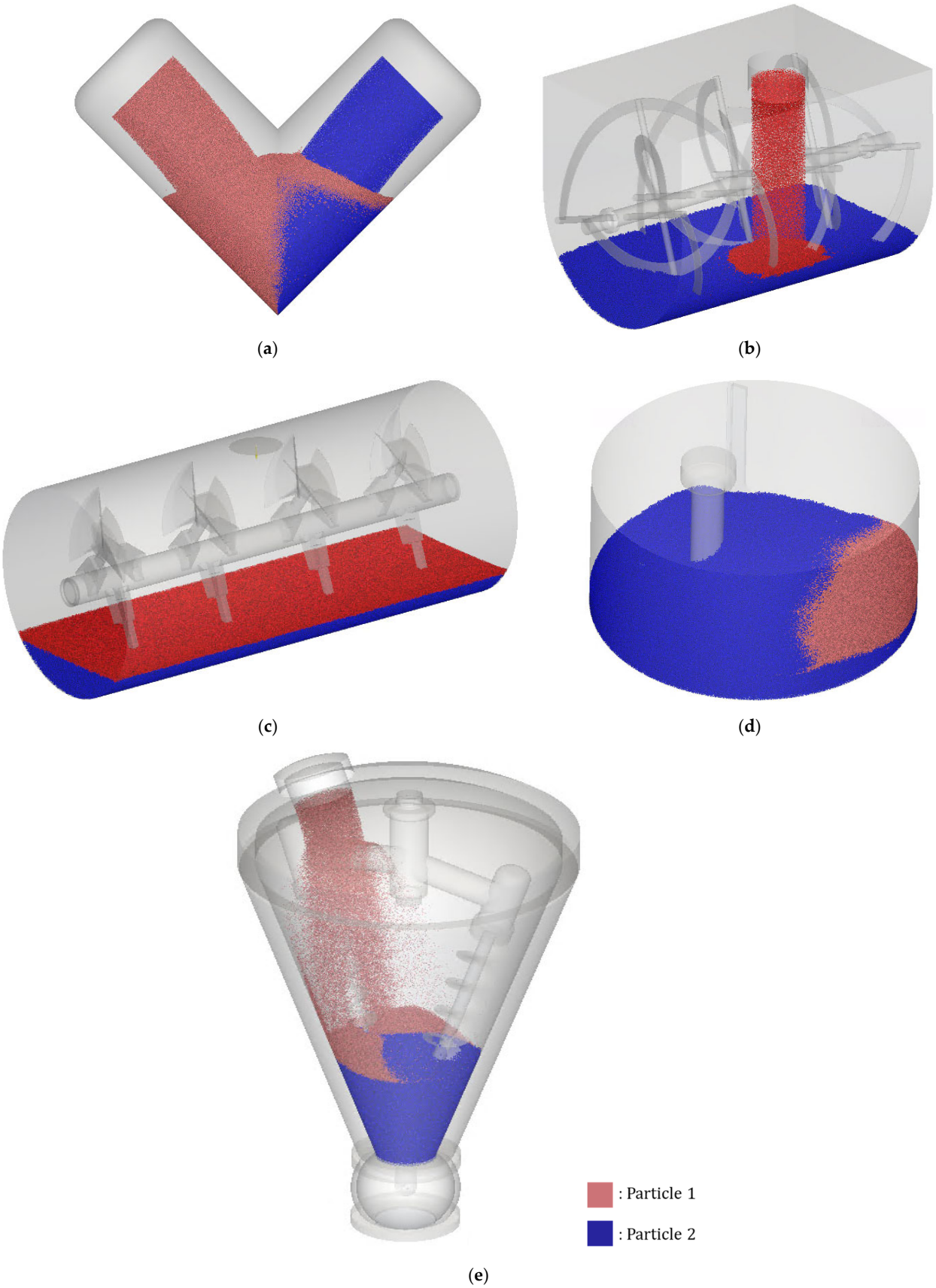

Figure 10. Initial spatial distributions of particles 1 and 2 before mixing: (**a**) tumbling V mixer; (**b**) ribbon-blade mixer; (**c**) paddle-blade mixer; (**d**) vertical-blade mixer; (**e**) conical-screw mixer.

Table 2. Particle sizes and masses for each mixing process.

Mixer Type	Diameter [mm]		Total Mass [kg]	
	Particle 1	Particle 2	Particle 1	Particle 2
Tumbling V mixer	3	6	180	100
Ribbon-blade mixer	2	4	11	110
Paddle-blade mixer	2	4	84	185
Vertical-blade mixer	1	2	3	75
Conical-screw mixer	2	4	200	250

4.2. LMI

The LMI, a statistical measure commonly used to evaluate the homogeneity of particle mixing, was employed in this study. It is defined as follows:

$$LMI = ({S_0}^2 - S^2)/({S_0}^2 - {S_R}^2), \quad (14)$$

$${S_0}^2 = \omega_{system}(1 - \omega_{system}), \quad (15)$$

$${S_R}^2 = \omega_{system}\frac{(1-\omega_{system})}{n}, \quad (16)$$

$$S^2 = \frac{1}{N-1}\sum_{i=1}^{N}(\omega_i - \bar{\omega})^2, \quad (17)$$

$$\omega_i = {m_{Additive,i}}/{m_{Additive,i} + m_{Main\ Product,i'}} \quad (18)$$

where ${S_0}^2$ represents the variance in a completely segregated state, S^2 is the variance in the current mixing state, ${S_R}^2$ is the variance in a fully randomized mixture, $\bar{\omega}$ is the average additive mass fraction across cells, ω_i is the average mass fraction in cell i, n is the average number of particles across cells, $m_{Additive,i}$ is the additive mass in cell i, and $m_{Main\ Product,i}$ is the main product mass in cell i [29]. The LMI has a value between 0 and 1, where 0 indicates complete segregation (i.e., no mixing has occurred), and 1 represents perfect mixing (i.e., particles are uniformly distributed throughout the system).

Lacey's approach represents a quantitative method for evaluating mixing efficiency. However, its physical meaning must be carefully interpreted due to certain limitations. Specifically, the LMI depends on the size and distribution of the sampling grid, which may lead to discrepancies between calculated values and the actual mixing state [30]. Moreover, in cases where component ratios are highly unbalanced or during the early stages of mixing, the LMI may exceed 1 or even exhibit negative values, which would necessitate careful interpretation [31].

Under certain CGM conditions, negative LMI values may appear during the initial mixing stages. Such values do not reflect any physically meaningful phenomenon but instead result from a statistical artifact inherent to the LMI formulation. Specifically, when the observed variance within sampling bins exceeds the theoretical variance of a fully randomized mixture, the computed LMI may temporarily become negative. This typically occurs in cases where the number of particles per bin is insufficient for robust statistical evaluation or when the initial particle distribution exhibits extreme segregation. To address this issue, bins containing fewer than 10 particles were excluded from the LMI calculation, which minimized statistical noise and ensured reliable quantification of mixing behavior.

The LMI values were calculated using a discretized spatial domain, divided into uniformly sized cubic cells. This approach provided an accurate measure of the local particle distributions and mixing uniformity throughout all mixing systems.

4.3. Sampling Zone Definition for LMI Calculation

To quantitatively assess mixing uniformity using the LMI, the internal domain of each mixing system was discretized into uniformly sized cubic cells. This discretization enabled the measurement of local particle compositions, which is essential for statistical variance calculations in LMI. We uniformly divided the internal volume of each mixer into regular-sized cubic cells, ensuring equal spatial resolution. The cell dimensions were determined based on each mixer's geometry to balance resolution with computational feasibility.

As mentioned earlier, only cells containing more than 10 particles during the sampling period were considered in the final variance calculation. This threshold removed sparsely populated zones, which could introduce statistical noise and distort the LMI values. Figure 11 shows representative examples of spatially subdivided mixing geometries. All cells in these figures are of equal size and represent the initial sampling zones prior to any filtering. The described spatial partitioning and filtering approach was consistently applied across all five mixing processes to ensure comparability and statistical reliability when evaluating mixing efficiency. Figure 12 presents the filtered sampling zones, highlighting only those regions that satisfy the particle-count threshold. This filtering strategy ensured that the LMI would reflect actual mixing behavior rather than being influenced by sparse or underpopulated regions.

This zone partitioning and filtering approach was consistently applied across all five mixing processes to maintain comparability and statistical reliability in the LMI evaluation.

To ensure meaningful statistical evaluation under varying CGM scaling conditions, the bin size used for spatial discretization was adjusted accordingly. In cases where the particle size increased due to coarse graining, using smaller bins led to many cells having insufficient particle counts, which would potentially compromise the reliability of the LMI calculations. Therefore, the bin size was scaled to ensure that most cells would contain more than 10 particles, thereby satisfying the threshold for inclusion in the LMI computation. Additionally, although the bin sizes varied across cases, the total particle mass involved in the LMI evaluation was consistently maintained to ensure a fair comparison. While a formal sensitivity analysis was not conducted, this sampling strategy was implemented to minimize numerical artifacts and ensure robust LMI-based mixing assessments.

The influence of the sampling resolution and bin size on the LMI accuracy is acknowledged to be an important factor and will be considered in future investigations.

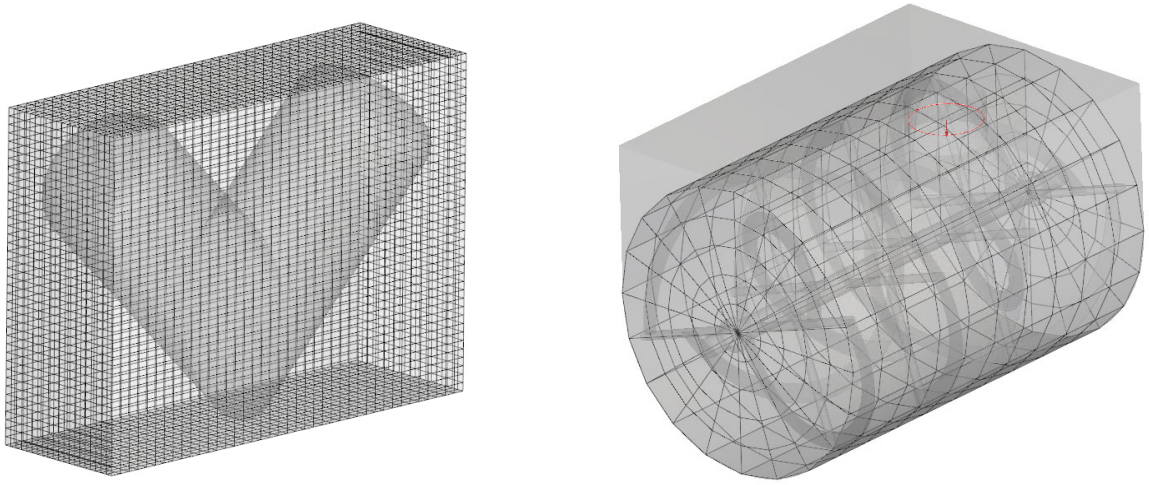

(**a**) (**b**)

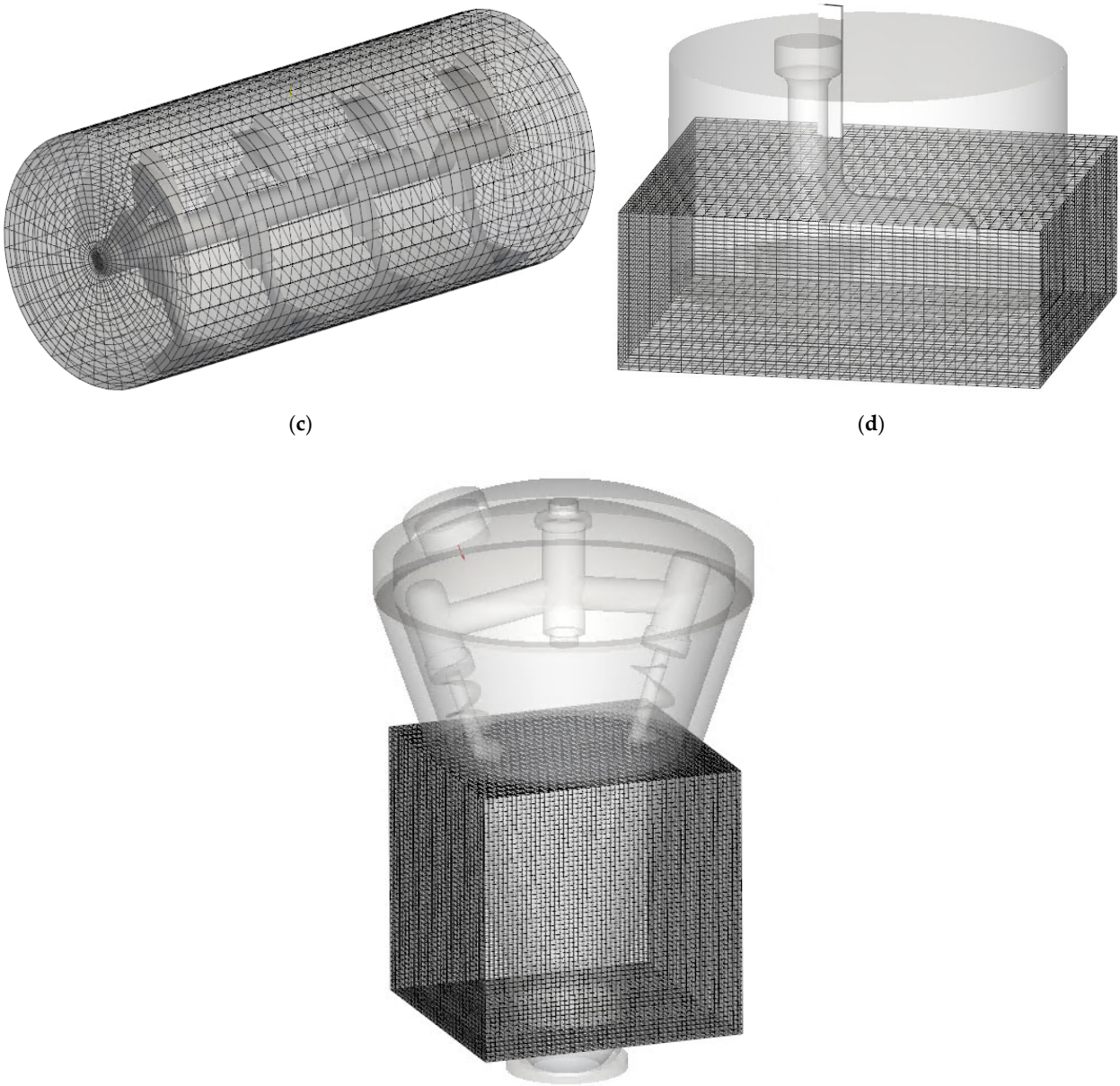

(**c**) (**d**)

(**e**)

Figure 11. Uniform cell-based spatial division of mixing domain: (**a**) tumbling V mixer; (**b**) ribbon-blade mixer; (**c**) paddle-blade mixer; (**d**) vertical-blade mixer; (**e**) conical-screw mixer.

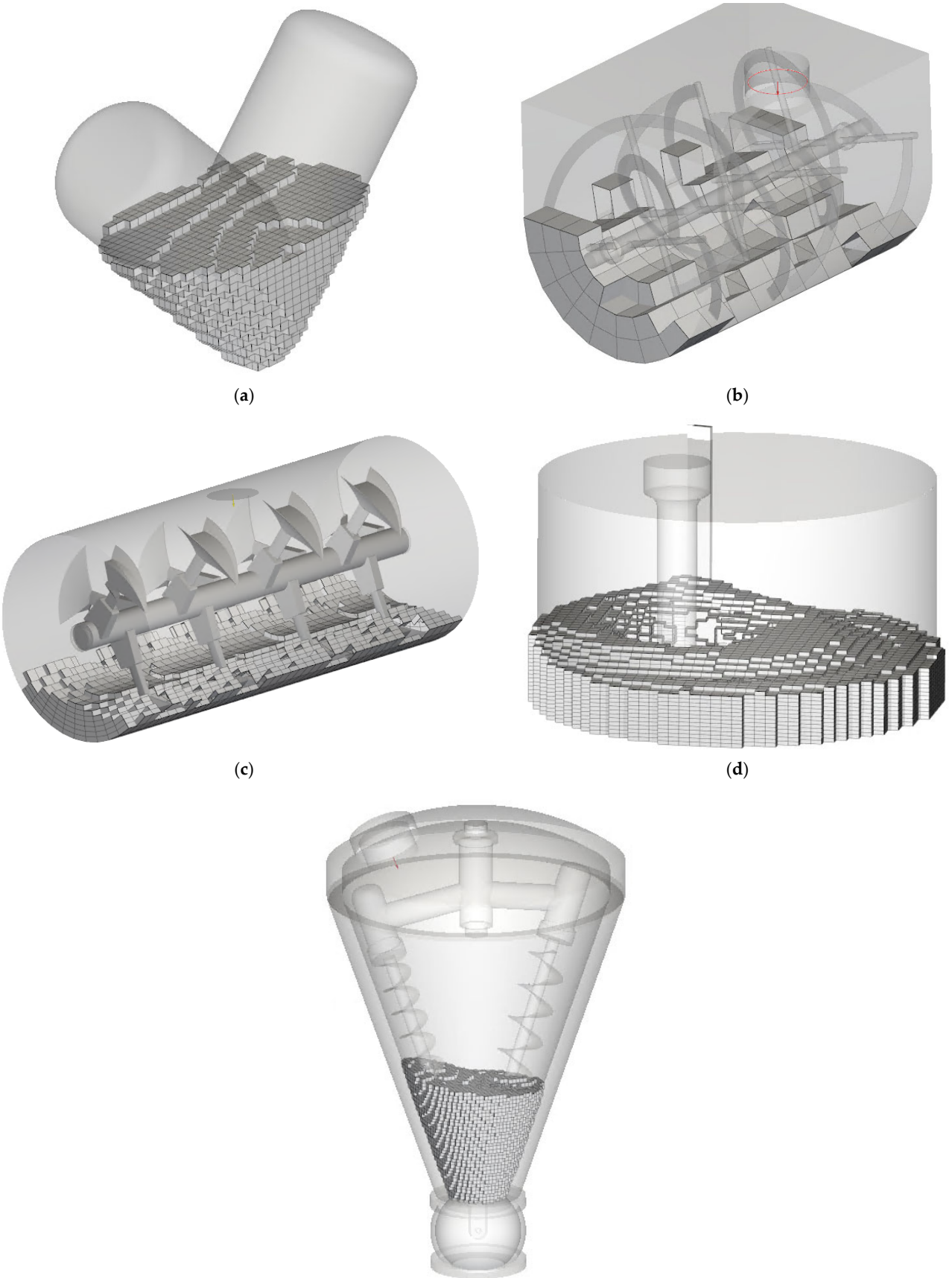

Figure 12. Sampling zones satisfying particle-count threshold (>10 particles per cell): (**a**) tumbling V mixer; (**b**) ribbon-blade mixer; (**c**) paddle-blade mixer; (**d**) vertical-blade mixer; (**e**) conical-screw mixer.

5. Numerical Analysis Results

This section presents the DEM simulation results for the five selected mixing processes, focusing on the impact of the CGM scaling factor on the mixing efficiency, quantified by the LMI. As the simulation setups for each mixing process are already described in the previous sections, they are not repeated here. Instead, emphasis is placed on interpreting the trends observed in the LMI and analyzing the influence of the CGM scaling factor on the mixing behavior. For each mixing system, the LMI was computed at regular intervals throughout the simulation to track its temporal evolution. Additionally, during the final second of the mixing process, statistical metrics, namely average, maximum, minimum, and standard deviation, were calculated for the LMI values to summarize the steady-state mixing performance. Representative snapshots of particle distributions were also captured at specific intervals to gain qualitative insights into the internal mixing states under varying CGM conditions.

5.1. Mixing Efficiency Analysis of Tumbling V Mixer with CGM Scaling

We analyzed the impact of various CGM scaling factors on the mixing efficiency in the tumbling V mixer, based on the DEM simulation results. Simulations were performed under six CGM conditions (CGM = 1, 2, 3, 4, 5, and 7). For each case, the temporal variation in the LMI and the evolution of the particle distributions were evaluated.

Figure 13 illustrates the temporal evolution of the LMI values across all CGM cases. While the absolute LMI values differed among the CGM levels, the general trends were consistent. Notably, the differences in the LMI values between the scaling levels tended to diminish over time, which indicates that the mixing behavior converged as the simulation progressed. Although the simulations were concluded before complete mixing was achieved, we anticipate that the deviations between the CGM cases would continue to diminish if the simulations were extended beyond 30 s.

Figure 14 displays the particle distributions at multiple time points for each CGM condition. Across all CGM levels, the macroscopic mixing patterns appeared visually consistent, which indicates that CGM scaling does not significantly alter the overall mixing behavior. However, simulations with finer CGM levels (e.g., CGM = 1) provided smoother and more detailed representations of the mixing interface, akin to high-resolution imaging. As the CGM factor increased, the granularity of the particle representation became coarser, slightly reducing visual clarity, although the overall mixing characteristics remained unchanged.

Table 3 presents the statistical metrics of the LMI (average, maximum, and minimum) during the final second of the simulation (29–30 s), along with the total number of particles, the simulation time, and the estimated error percentages. The results demonstrate that increasing the CGM factor substantially reduced the computational time by more than two orders of magnitude, while maintaining the LMI error within an acceptable range. We expect that prolonged simulation would reduce the error even further, which highlights the practical advantages of CGM for large-scale simulations. In Table 3, the error is defined as the absolute difference between the average LMI value of each CGM case and the non-CGM case (CGM = 1), expressed as a percentage. This definition is used consistently throughout the following subsections.

For the tumbling V mixer, the LMI error exceeded 10% in most CGM cases, with the highest observed deviations surpassing 16%. Even the lowest-error case (CGM = 7) showed a non-negligible deviation of 8.56%. These elevated errors are attributed to the fact that the system had not yet reached a sufficiently mixed state by the end of the simulation, as reflected in the relatively low final LMI of approximately 0.300 in the non-CGM case. To investigate this trend further, we conducted additional comparisons at earlier time intervals (i.e., 25–26 s and 27–28 s). The results indicate a progressive decrease in the

error over time, suggesting that the high errors observed at 29–30 s are likely transient effects of incomplete mixing. These results are summarized in Table 4, which presents the LMI values and the corresponding error percentages across multiple-time windows and CGM levels.

Table 3. Particle counts, simulation times, LMI statistics, and errors for the Tumbling V mixer.

	W/O CGM	CGM Scaling Factor				
		2	3	4	5	7
Particle count	4.53×10^6	5.66×10^5	1.68×10^5	7.07×10^4	3.62×10^4	1.32×10^4
Simulation duration	58 h 30 min	7 h 45 min	1 h 23 min	39 min	24 min	13 min
Average LMI	0.300	0.330	0.343	0.347	0.335	0.324
Minimum LMI	0.289	0.321	0.328	0.332	0.322	0.304
Maximum LMI	0.305	0.338	0.350	0.345	0.344	0.337
Error	–	10.40%	14.71%	16.15%	12.13%	8.56%

Table 4. LMI error trends for the Tumbling V mixer at CGM factors 2–7 over time.

Time (s)	W/O CGM	CGM Scaling Factor				
		2	3	4	5	7
25~26	-	21.60%	35.79%	38.83%	33.92%	23.13%
27~28	-	18.29%	26.38%	27.69%	20.45%	14.75%
29~30	-	10.40%	14.71%	16.15%	12.13%	8.56%

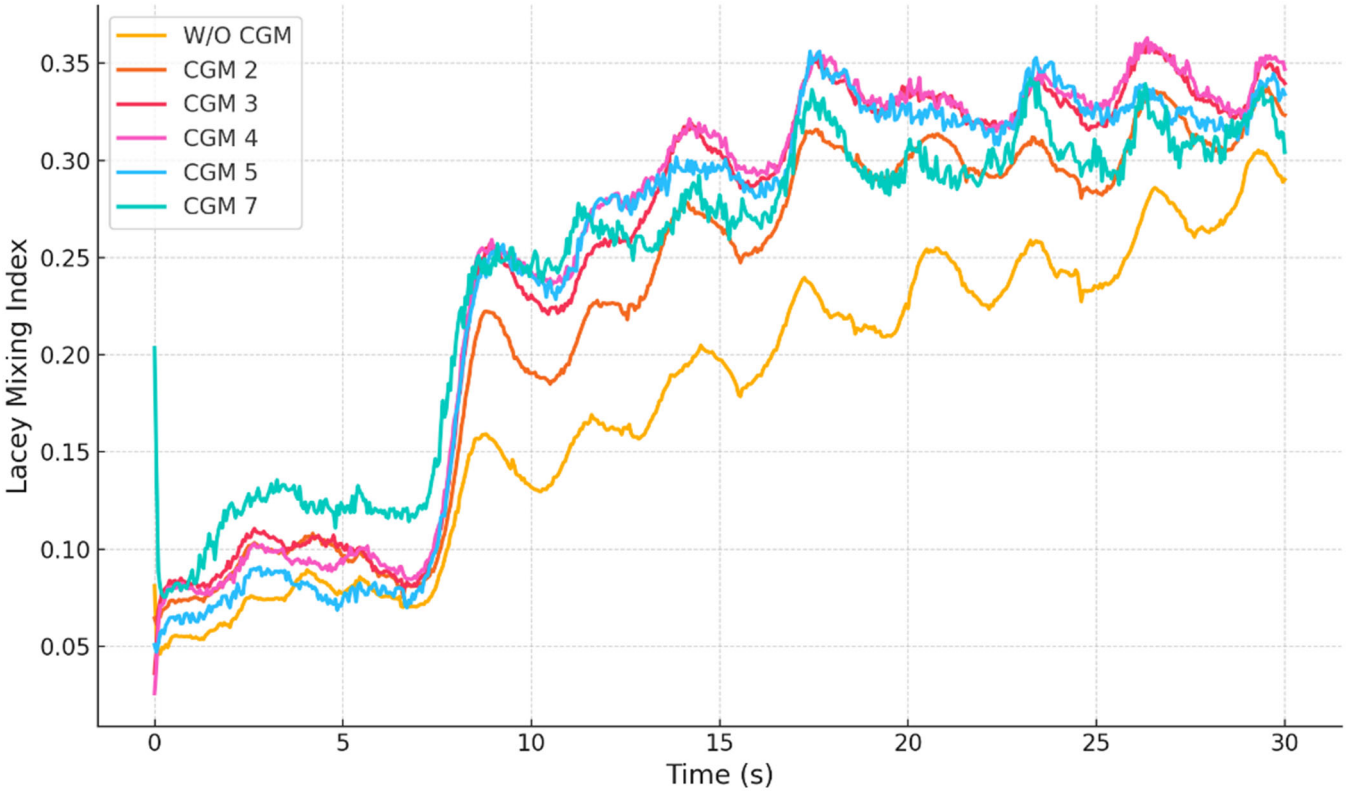

Figure 13. Temporal evolution of LMI for the Tumbling V mixer.

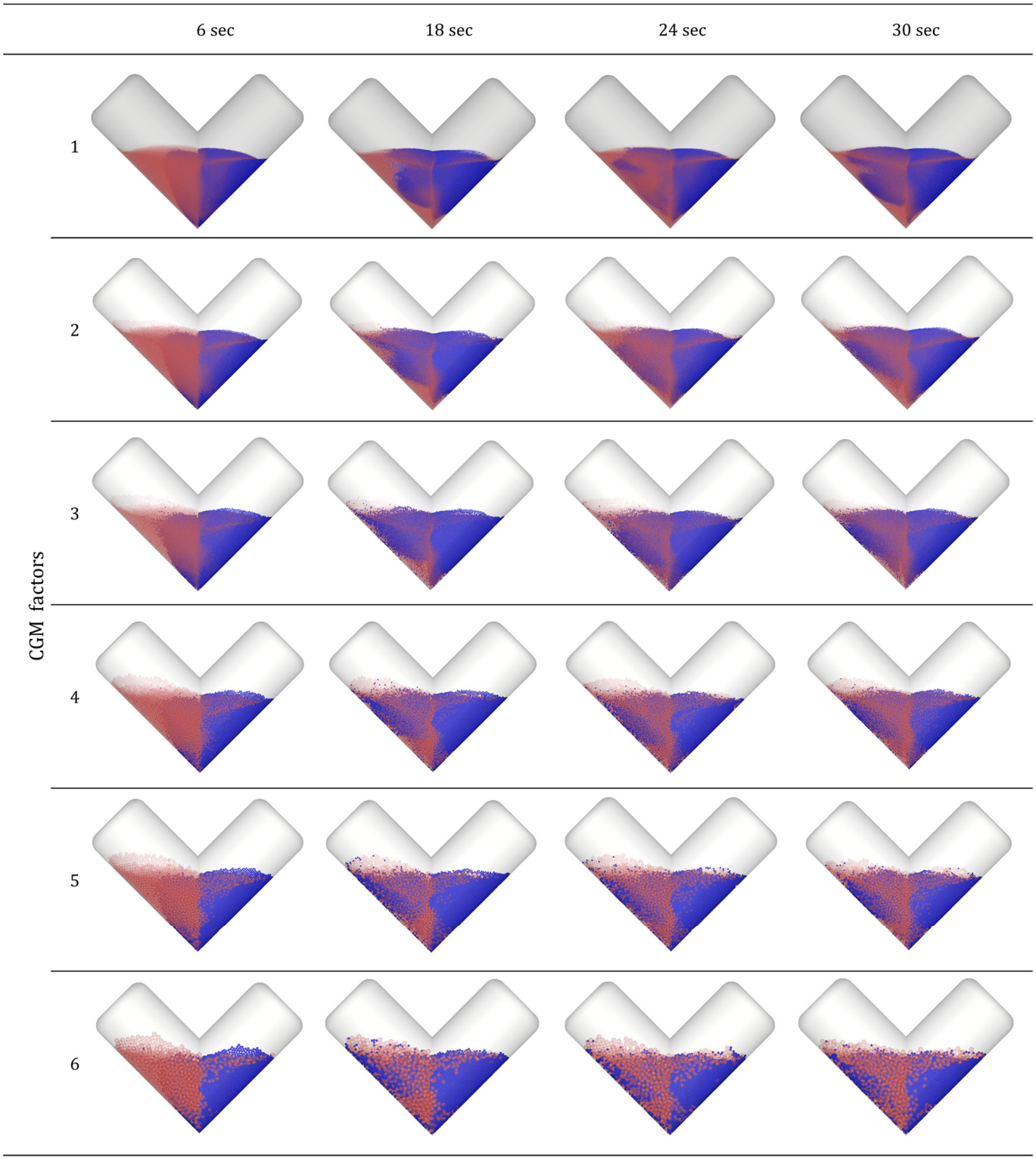

Figure 14. Particle distribution snapshots under different CGM conditions in the Tumbling V Mixer.

5.2. Mixing Efficiency Analysis of Ribbon-Blade Mixer with CGM Scaling

This section presents the DEM simulation results for the ribbon-blade mixer under various CGM conditions (CGM = 1, 2, 3, 4, 5, 7, and 10). The analysis included particle distribution snapshots, the temporal evolution of the LMI, and statistical summaries during the final simulation phase.

Figure 15 illustrates the temporal evolution of the LMI. A rapid increase was observed within the first 10 s, followed by convergence near 1 across all CGM conditions. Although slight fluctuations occurred, the overall trends remained similar, regardless of

the CGM level. Notably, the LMI deviation across CGM levels diminished over time, which suggests that further simulation would likely lead to even greater convergence.

Figure 16 shows the particle distributions at 6, 18, 24, and 30 s for different CGM levels. While the visual detail varied with the particle resolution, the general mixing trends remained consistent. Finer CGM levels (e.g., CGM = 1) provided smoother and more continuous depictions of particle layers and transitions, whereas coarser levels (e.g., CGM = 10) resulted in a more clustered and granular appearance. Nonetheless, all CGM conditions ensured effective mixing by the end of the simulation.

Table 5 summarizes the key metrics, including the particle counts, total simulation time, and LMI values (average, maximum, and minimum) during the final second of mixing. The CGM factor significantly influenced the simulation time, with CGM = 10 reducing the total computation from 125 h to only 14 min. Despite this drastic reduction, the LMI error remained under 5.6% across all scaling factors. These results confirm that CGM yields substantial computational savings while maintaining acceptable accuracy. Extending the simulation is expected to enhance the LMI convergence and reduce the error margins further.

Table 5. Particle counts, simulation times, LMI statistics, and errors for the Ribbon-Blade Mixer.

	W/O CGM	**CGM Scaling Factor**					
		2	**3**	**4**	**6**	**7**	**10**
Particle count	2.71×10^6	3.38×10^5	9.84×10^4	4.07×10^4	2.04×10^4	7.16×10^3	2.28×10^3
Simulation duration	125 h	4 h	1 h 20 min	40 min	30 min	20 min	14 min
Average LMI	0.972	0.970	0.963	0.955	0.949	0.918	0.928
Minimum LMI	0.973	0.973	0.975	0.973	0.972	0.963	0.978
Maximum LMI	0.971	0.963	0.926	0.896	0.899	0.831	0.824
Error	–	0.18%	0.92%	1.74%	2.32%	5.58%	4.49%

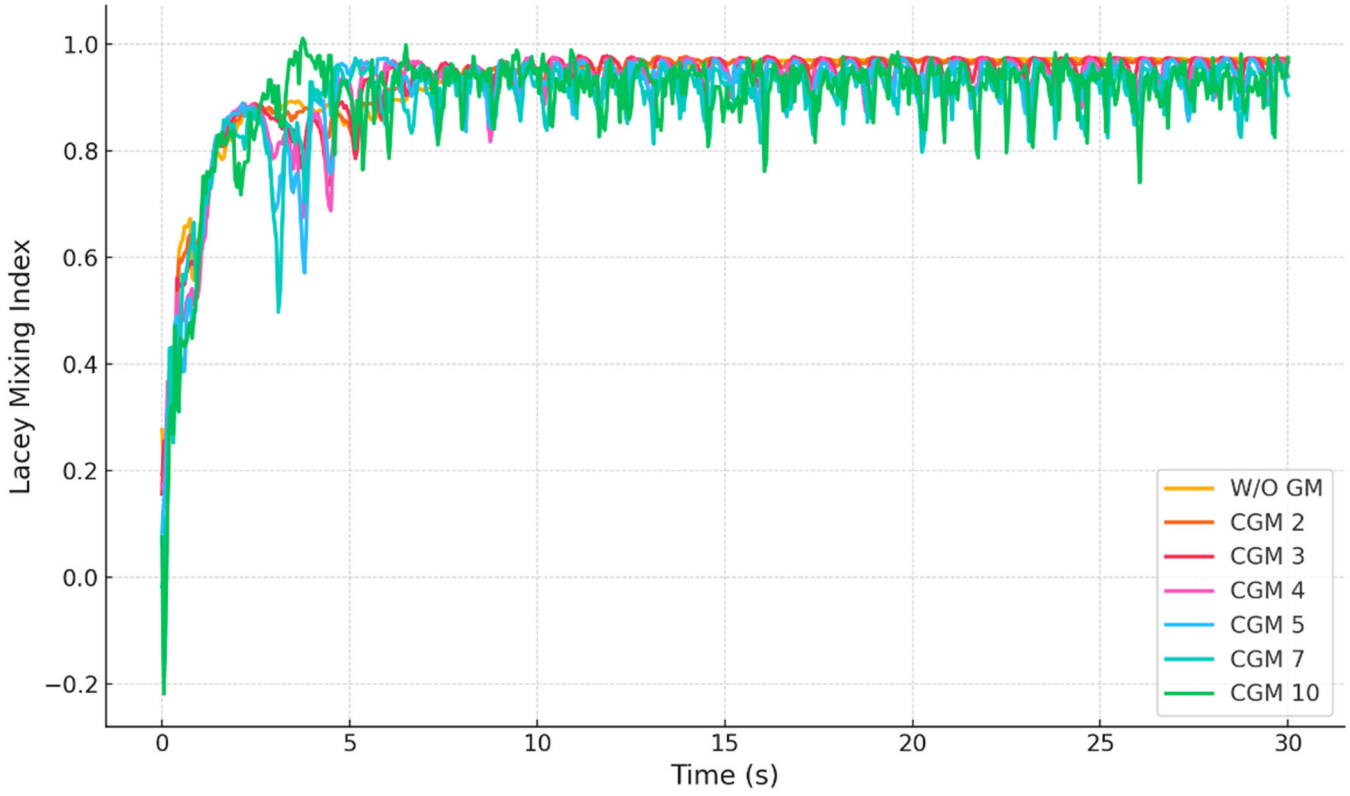

Figure 15. Temporal evolution of LMI for different CGM factors for the Ribbon-Blade Mixer.

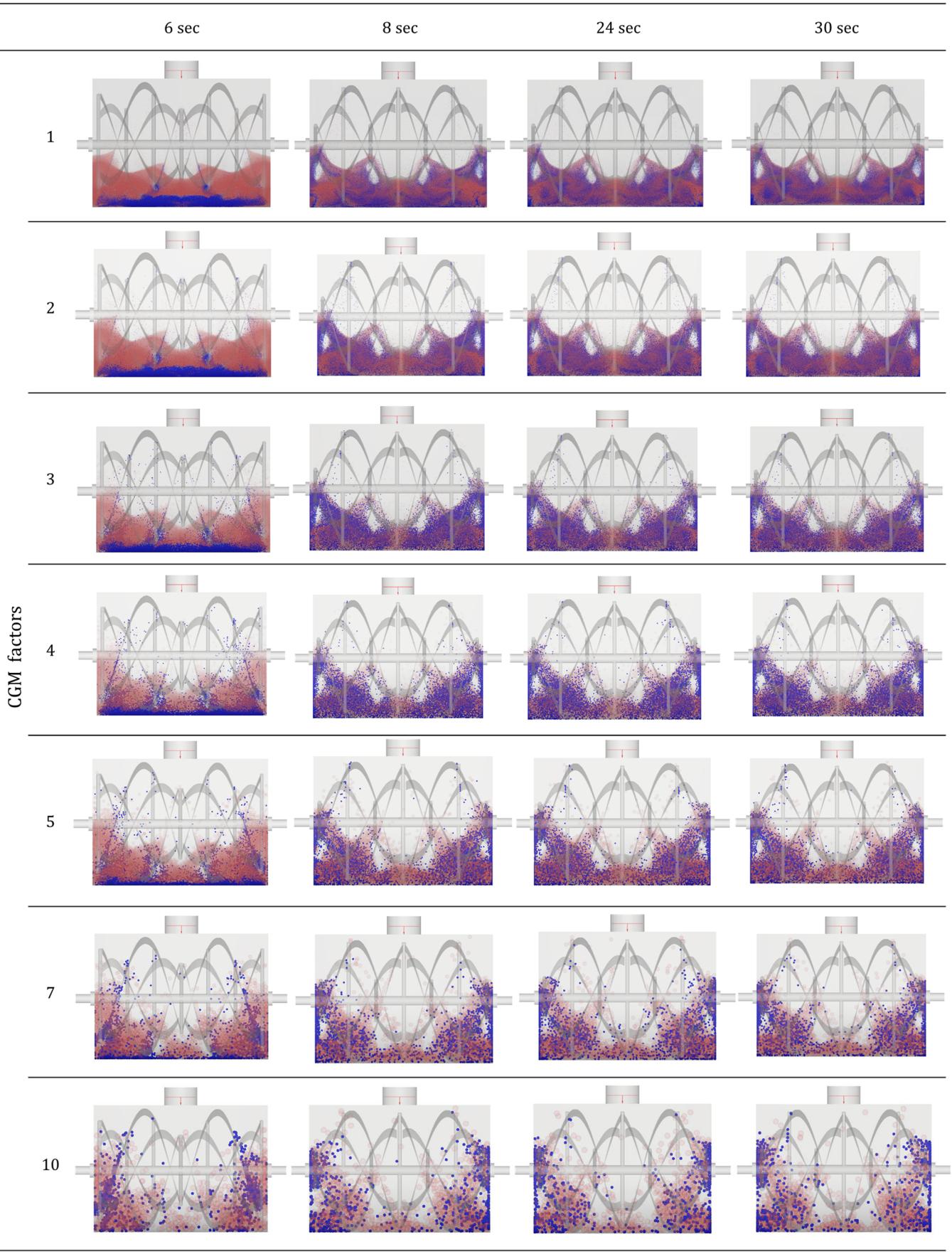

Figure 16. Particle distribution snapshots in the Ribbon-Blade Mixer (CGM = 1–10).

5.3. Mixing Efficiency Analysis of Paddle-Blade Mixer with CGM Scaling

This section presents the DEM simulation results for the paddle-blade mixer under various CGM scaling factors (CGM = 1, 2, 3, 4, 5, and 7). The analysis focused on changes in the particle distribution over time, the temporal behavior of the LMI, and a comparison of the statistical LMI metrics and computational time during the final second of the simulation.

Figure 17 shows the time evolution of the LMI. During the early phase of mixing, variations in the rate of increase and stabilization of LMI are evident depending on the CGM level. Nevertheless, the general trends converged along a similar trajectory. Particularly for CGM values of 4 and higher, a rapid improvement in mixing was observed, with the absolute differences in the LMI between the CGM conditions gradually diminishing over time. Figure 18 presents snapshots of the particle distributions at 6, 18, 24, and 30 s for each CGM condition. As the CGM factor increased, the number of particles decreased; however, the overall mixing patterns remained consistent. In the high-resolution case (CGM = 1), the mixing interface appeared smoother and more continuous, with similar spatial distribution trends being observed even at CGM = 7.

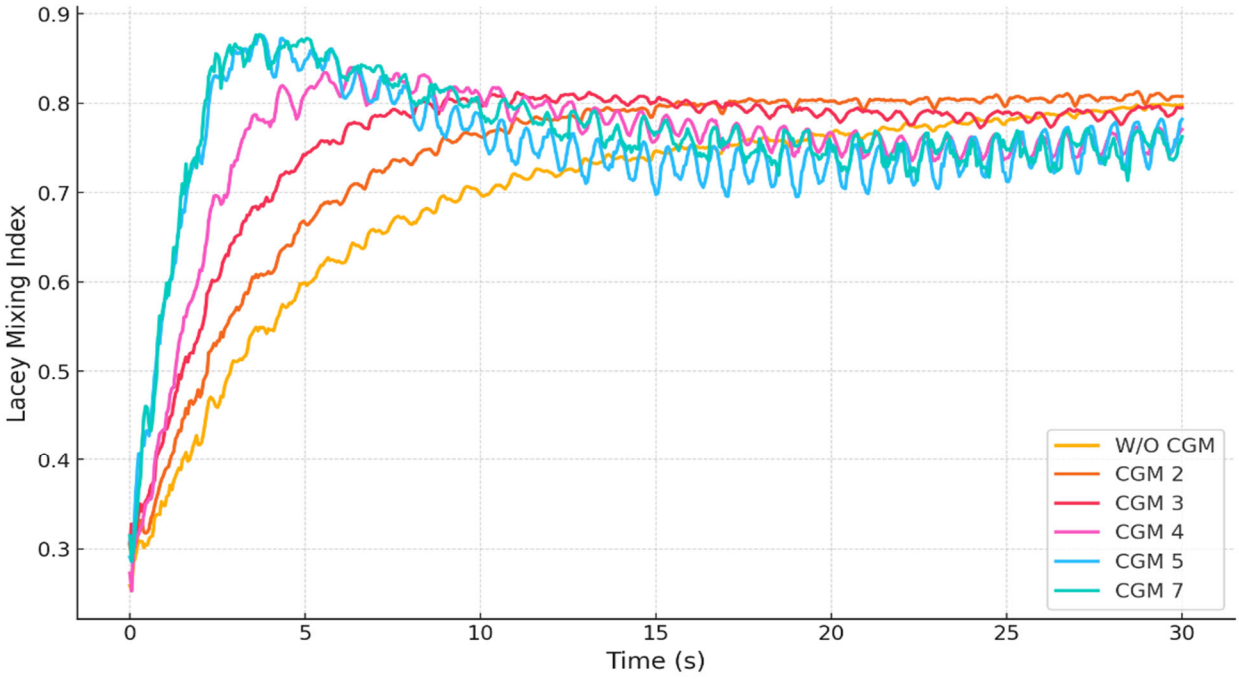

Figure 17. Temporal evolution of LMI for different CGM factors for the Paddle-Blade Mixer.

Table 6 summarizes the average, maximum, and minimum LMI values during the final second of mixing (29–30 s), along with the particle count, total simulation time, and percentage error for each CGM case. As the CGM factor increased, the simulation time was significantly reduced, from 186 h for CGM = 1 to only 26 min for CGM = 7. The error rates remained low for CGM = 2 (1.18%) and CGM = 3 (0.64%); even at higher CGM values, the errors remained within 5.5%. These findings emphasize the effectiveness of CGM in improving computational efficiency substantially while maintaining reliable physical accuracy.

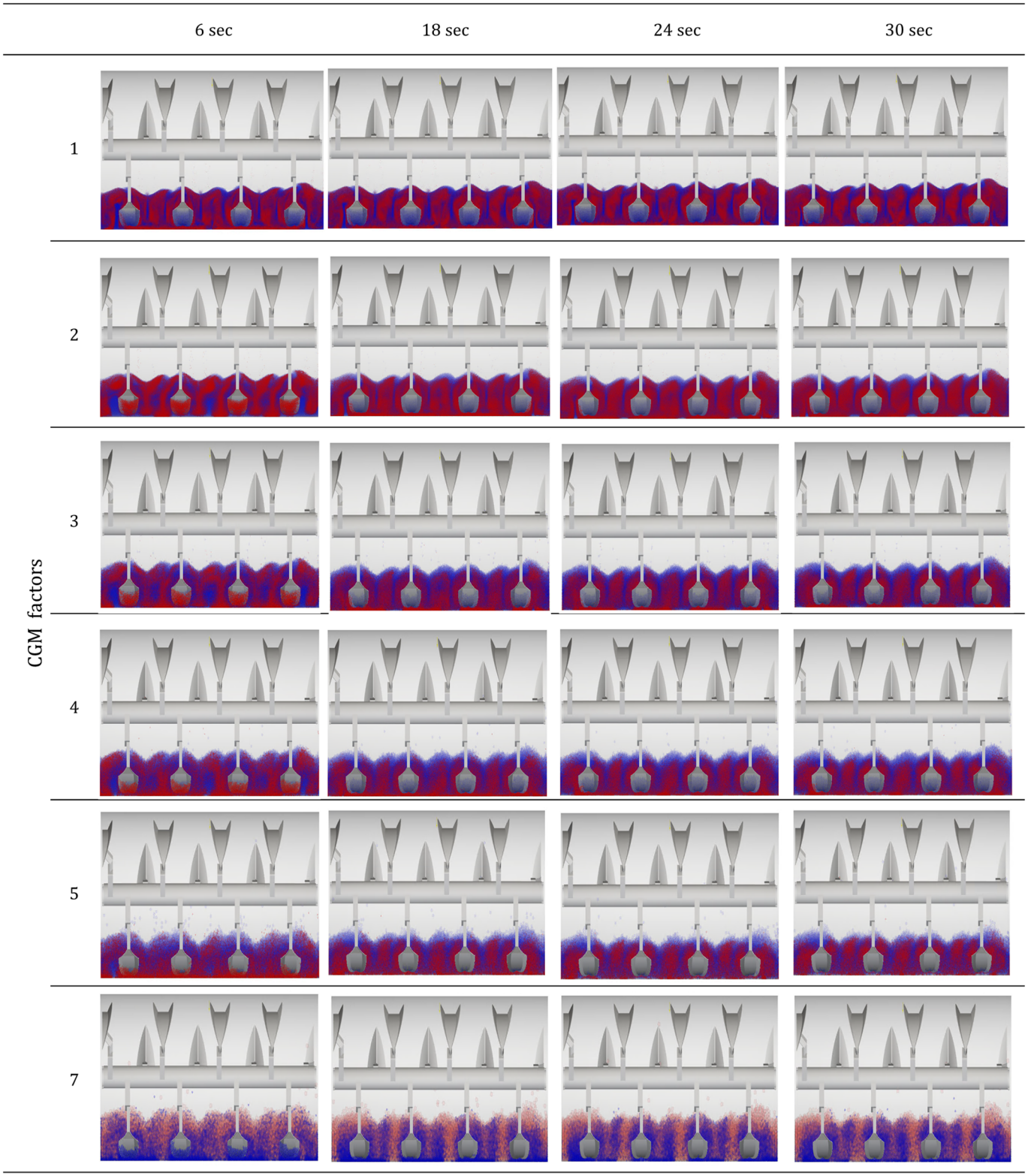

Figure 18. Particle distribution snapshots at 6, 18, 24, and 30 s under various CGM factors in the Paddle-Blade Mixer.

Table 6. Particle counts, simulation times, LMI statistics, and errors for the Paddle-Blade Mixer.

	W/O CGM	CGM Scaling Factor				
		2	3	4	5	7
Particle count	9.85×10^6	1.27×10^6	3.78×10^5	1.36×10^5	6.66×10^4	2.97×10^4
Simulation duration	186 h	12 h	2 h 35 min	1 h 13 min	41 min	26 min
Average LMI	0.798	0.807	0.793	0.758	0.760	0.754
Minimum LMI	0.799	0.811	0.797	0.772	0.782	0.771
Maximum LMI	0.795	0.801	0.785	0.742	0.726	0.736
Error	–	1.18%	0.64%	4.98%	4.81%	5.51%

5.4. Mixing Efficiency Analysis of Vertical-Blade Mixer with CGM Scaling

This section presents the DEM simulation results for the vertical-blade mixer under various CGM scaling factors (CGM = 1, 2, 3, 4, and 5). The analysis focused on the evolution of the particle-mixing characteristics over time, the quantitative changes in the LMI, and statistical summaries from the final second of each simulation.

Figure 19 presents the temporal evolution of the LMI. While differences in absolute values were observed across CGM factors, the LMI consistently increased over time under all conditions. During the initial mixing phase, some CGM cases showed negative LMI values, which is attributed to the statistical nature of the LMI formula. Such values can arise when the component ratio is highly unbalanced or when sampling is insufficient in the early stages. Nevertheless, the LMI values across all CGM cases increased along similar trajectories and began converging as the mixing progressed, which reinforces the robustness of LMI-based evaluation.

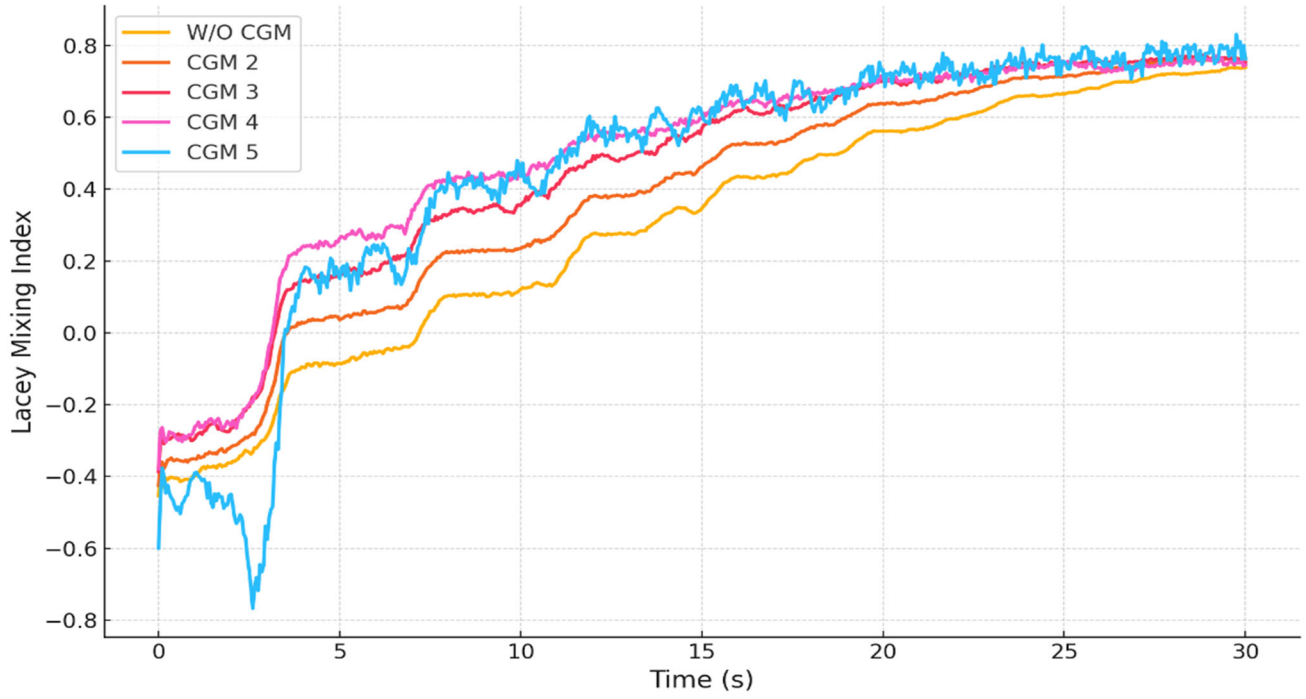

Figure 19. Time evolution of the LMI for different CGM factors for the Vertical-Blade Mixer.

Figure 20 presents the particle distribution snapshots at 6, 18, 24, and 30 s for each CGM condition. The overall mixing pattern remained consistent across all CGM levels. Although the resolution of individual particles decreased with higher CGM scaling, the general flow behavior and mixing characteristics exhibited minimal deviation. This confirms that the underlying mixing mechanisms are preserved even after CGM.

As shown in Figure 19, extending the simulation would likely have led to further convergence of the LMI values across CGM conditions, potentially reducing the error margins. Table 7 summarizes the average, maximum, and minimum LMI values during the 29–30 s interval, along with the particle count, total simulation time, and error percentage for each CGM case. As the CGM scaling increased, the simulation time was significantly reduced, from approximately 500 h at CGM = 1 to only 3 h and 7 min at CGM = 5. The error rates largely remained within 4%, which indicates that CGM can ensure reliable numerical accuracy while providing substantial computational savings.

The negative LMI values observed during the early stages in certain CGM cases can be interpreted based on the unique flow characteristics of the vertical-blade mixer. Due to the high-speed rotation of the central vertical blade, strong centrifugal forces are generated near the core region, which mobilize the central particles. Meanwhile, the peripheral regions near the vessel wall may remain relatively stagnant. If the initial particle arrangement is inhomogeneous, especially with clusters near the wall, these dead zones can temporarily persist, causing the particle distributions to be more segregated than in a purely random state. As mixing progresses, however, these stagnant regions are gradually eliminated, and the LMI returns to physically meaningful levels.

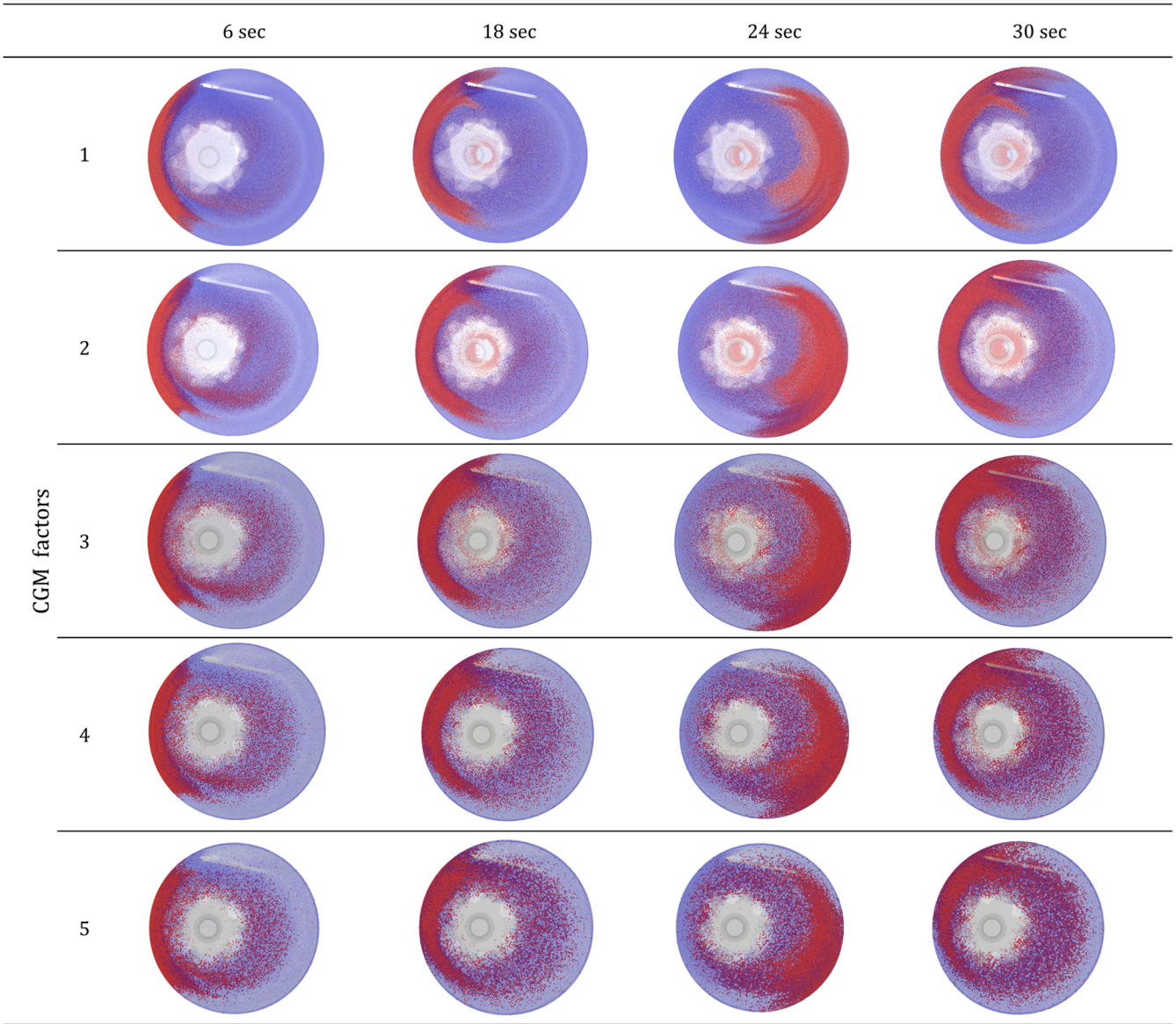

Figure 20. Particle distribution snapshots at 6, 18, 24, and 30 s under various CGM factors in the Vertical-Blade Mixer.

Table 7. Particle counts, simulation times, LMI statistics, and errors for the Vertical-Blade Mixer.

	W/O CGM	CGM Scaling Factor			
		2	3	4	5
Particle count	8.93×10^6	1.12×10^6	3.30×10^5	1.39×10^5	7.14×10^4
Simulation duration	500 h	70 h	13 h 20 min	4 h 27 min	3 h 7 min
Average LMI	0.734	0.762	0.762	0.755	0.785
Minimum LMI	0.739	0.766	0.767	0.771	0.831
Maximum LMI	0.727	0.756	0.753	0.742	0.749
Error	–	3.84%	3.86%	2.88%	6.95%

5.5. Mixing Efficiency Analysis of Conical-Screw Mixer with CGM Scaling

This section presents the DEM simulation results for the conical-screw mixer under various CGM scaling factors (CGM = 1, 2, 3, 4, 5, and 7). We analyzed the mixing efficiency across different CGM conditions based on the time-dependent particle behavior and the LMI. The results are presented through particle distribution visualizations, LMI time-series plots, and statistical summaries for the final second of each simulation.

Figure 21 presents the temporal evolution of the LMI. In the early stages of mixing, fluctuations or negative LMI values were observed in some CGM cases. These anomalies are attributable to the statistical nature of the LMI formula, especially when the sample size is small or the composition is significantly imbalanced. Despite such early irregularities, all CGM cases demonstrated a steady upward trend in LMI over time, and values converged as mixing progressed. The overall LMI improvement pattern was similar across CGM levels, which confirms that adequate mixing performance can be achieved even at higher CGM values.

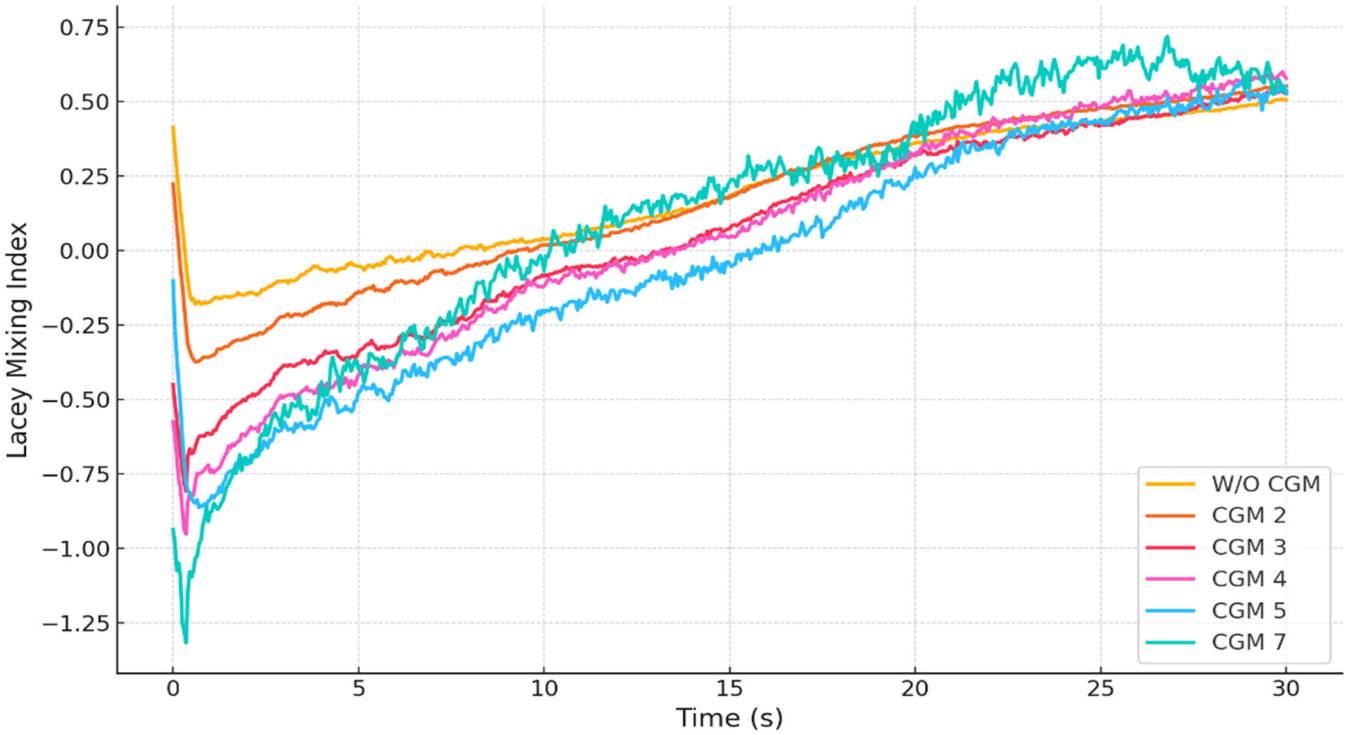

Figure 21. Temporal evolution of LMI for different CGM factors for the Conical-Screw Mixer.

Figure 22 displays the particle distributions at 6, 18, 24, and 30 s for each CGM level. Across all CGM conditions, the overall particle flow and mixing patterns remained visually consistent. Although the particle resolution decreased as the CGM factor increased,

the general mixing structure was preserved. This visual consistency supports the conclusion that the fundamental mixing mechanism is retained even after CGM.

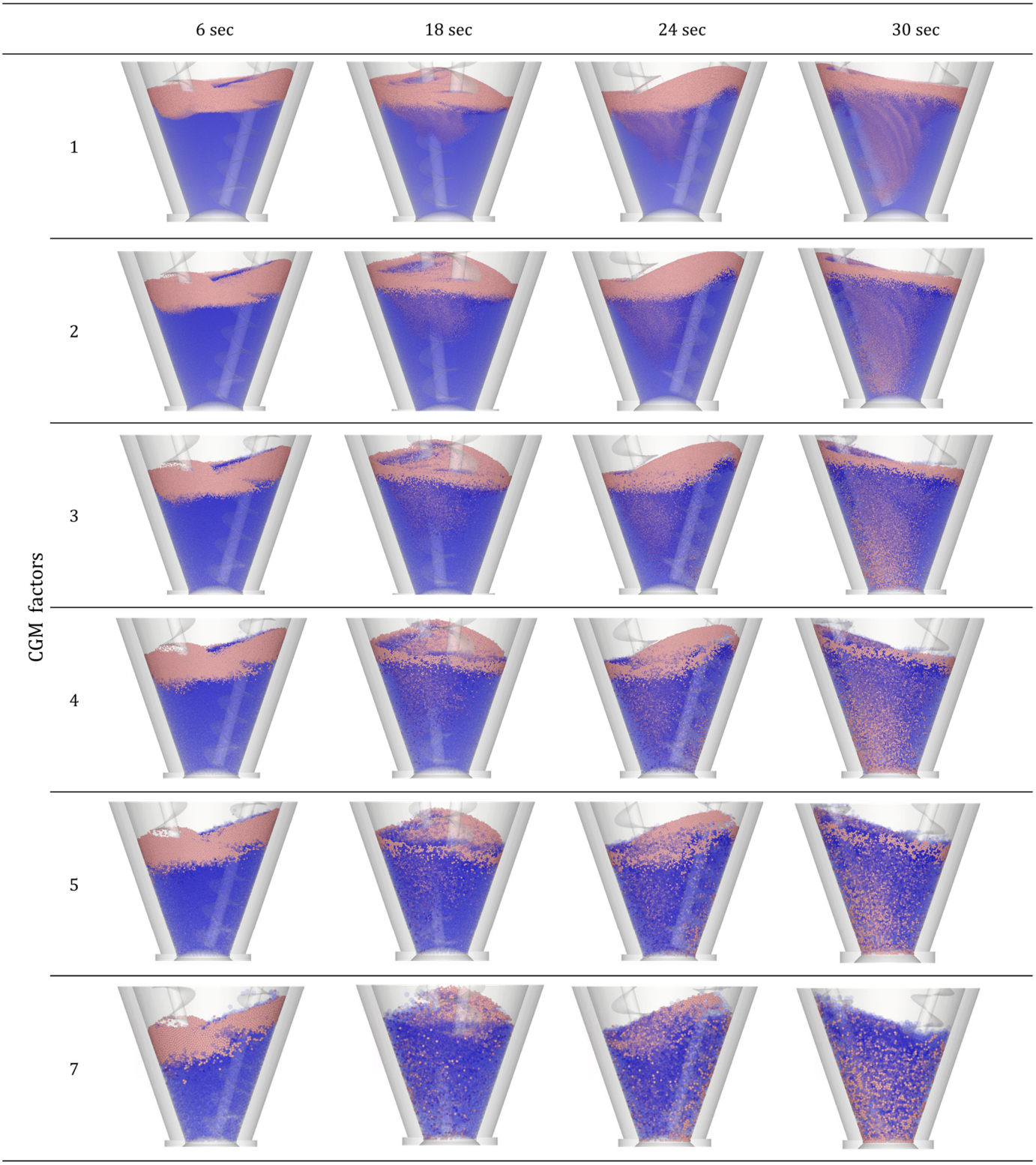

Figure 22. Particle distribution snapshots at 6, 18, 24, and 30 s under various CGM factors in the Conical-Screw Mixer.

As inferred from Figure 21, extending the simulation would likely have resulted in further convergence of LMI values across CGM conditions, which would reduce the error margins. Table 8 summarizes the particle count, total simulation time, and the average,

maximum, and minimum LMI values during the final second (29–30 s), along with the calculated error for each CGM condition. As the CGM factor increased, the simulation time was dramatically reduced, from approximately 114 h at CGM = 1 to only 30 m at CGM = 7. While the error varied among the CGM cases, it was relatively high under certain conditions. However, extending the simulation is expected to reduce these discrepancies further. These findings confirm the effectiveness of CGM in enhancing computational efficiency while maintaining the reliability of mixing performance evaluations.

Table 8. Particle counts, simulation times, LMI statistics, and errors for the Conical-Screw Mixer.

	W/O CGM	CGM Scaling Factor				
		2	3	4	5	7
Particle count	5.08×10^6	6.36×10^5	1.88×10^5	7.94×10^4	4.07×10^4	1.48×10^4
Simulation duration	114 h	8 h 16 min	2 h 36 min	1 h 18 min	48 min	30 min
Average LMI	0.568	0.546	0.526	0.584	0.527	0.576
Minimum LMI	0.576	0.553	0.540	0.601	0.555	0.635
Maximum LMI	0.559	0.533	0.514	0.572	0.472	0.525
Error	–	3.96%	7.40%	2.70%	7.28%	1.37%

The occurrence of negative LMI values during the early simulation stages can be explained by the specific dynamics of the conical-screw mixer. Due to the combined effects of orbital motion and multi-axis screw rotation, the initial flow field is highly asymmetric. Specifically, particles near the outer cone wall tend to move slowly in the vertical direction, whereby a stratified distribution is maintained. When particles are initially layered or segregated in this manner, the system can temporarily exhibit more structured heterogeneity than a purely random mixture, which leads to negative LMI values. As mixing continues and the screw mechanism circulates material through the entire domain, these structured layers gradually dissolve, and the LMI converges toward positive, physically meaningful levels.

5.6. Summary of Results

To enhance the clarity of comparative analysis, a summary of all simulated cases and their corresponding results is provided in Table 9. This table includes the total particle counts, simulation durations, average Lacey Mixing Index (LMI) values, and LMI-based errors for each mixer type.

The data clearly demonstrates that CGM significantly reduced the number of particles and computational time, often by over 90%, while maintaining acceptable LMI accuracy. In most cases, the average error in LMI remained within 5%, confirming the practical applicability of CGM for large-scale DEM simulations.

Notably, the ribbon blade mixer achieved the highest final LMI (0.972) and the lowest error (2.54%), whereas the tumbling V mixer showed the lowest final LMI (0.300) and the highest error (12.39%). These trends suggest that mixing systems with inherently strong macroscopic flow features are generally less sensitive to CGM-induced simplification.

Table 9. Summary of simulation results for all mixer types.

	Particle Count		Simulation Duration		Average LMI		Average
	W/O CGM	CGM Factor 7	W/O CGM	CGM Factor 7	W/O CGM	CGM Factor 7	Error
Tumbling V mixer	4.53×10^6	1.32×10^4	58.5 h	13 min	0.300	0.324	12.39%
Ribbon-blade mixer	2.71×10^6	2.28×10^3	125 h	14 min	0.972	0.928	2.54%
Paddle-blade mixer	9.85×10^6	2.97×10^4	186 h	26 min	0.798	0.754	3.42%
Vertical-blade mixer	8.93×10^6	7.14×10^4	500 h	3 h 7 min	0.734	0.785	4.38%
Conical-screw mixer	5.08×10^6	1.48×10^4	114 h	30 min	0.568	0.576	4.54%

6. Conclusions

This study systematically evaluated the applicability and accuracy of CGM in DEM simulations across five representative industrial mixers: a tumbling V mixer, a ribbon-blade mixer, a paddle-blade mixer, a vertical-blade mixer, and a conical-screw mixer. By increasing the particle size through CGM, the computational demands were significantly reduced, which enabled efficient large-scale simulations. However, such upscaling can introduce inaccuracies in mixing behavior predictions, particularly during the early stages of particle motion. To assess mixing performance, we analyzed the temporal variation in the LMI under various CGM scaling conditions.

For all five mixing systems, CGM yielded a substantial reduction in computational time, often exceeding 90%, while maintaining acceptable levels of LMI accuracy. Visual inspection of particle distributions and temporal LMI trends confirmed that the overall mixing patterns remained consistent across CGM conditions. Although early-stage discrepancies in the LMI were observed, especially at higher CGM values, these differences diminished as the simulations progressed. In many cases, the final LMI errors were limited to 5%, with negligible impact on the overall interpretation of mixing performance.

These results demonstrate that CGM is a reliable and efficient strategy for DEM-based mixing simulations, especially when full-resolution simulations are computationally prohibitive. CGM facilitates the modeling of entire mixing systems rather than limited domains, enabling more comprehensive process analysis and design optimization. Moreover, by quantifying the trade-off between accuracy and computational efficiency, this study provides valuable guidance for selecting appropriate CGM levels for specific mixing scenarios.

Beyond using fixed CGM values, more generalizable guidelines may be derived by considering the relative sizes of the particles and the mixing equipment. For example, in mixers with chambers spanning several meters in diameter, regardless of whether the particle size is on the order of a few microns or several millimeters, the global mixing behavior is typically governed more by macroscopic flow patterns than by individual particle trajectories. From this perspective, a coarse-graining approach remains valid across a wide range of CGM factors, provided that local-scale effects do not control the mixing mechanism. Therefore, the appropriate CGM value should be selected based on the characteristic ratio of the particle size and the mixer dimensions, as well as the accuracy required for the target application. While some local deviations may arise with higher CGM levels, the global trends and statistical mixing indices such as the LMI should remain largely unaltered.

A cross-comparison of the final LMI values and the average CGM-induced errors across all mixers revealed a clear trend. The ribbon-blade mixer achieved the highest final LMI (=0.970) with the lowest average error (=2.54%), followed by the paddle-blade mixer (LMI ≈ 0.798, error ≈ 3.42%) and the vertical-blade mixer (LMI ≈ 0.734, error ≈ 4.38%). The conical-screw mixer exhibited a lower LMI (=0.568) and a slightly higher average error (=4.54%). In contrast, the tumbling V mixer displayed the lowest LMI (=0.300) and the highest CGM-related errors across all cases. While a definite causal relationship was not identified, these results suggest that systems achieving higher degrees of mixing are generally less sensitive to CGM scaling, possibly due to the dominant role of macroscopic flow patterns in homogenized conditions.

Despite the pertinent findings, however, this study has several inherent limitations. First, all simulations were conducted using non-cohesive, spherical particles. While this modeling choice ensured computational efficiency and consistency, it disregarded inter-particle cohesion and shape-related effects, such as interlocking, angularity, and anisotropic flow resistance, which may influence local mixing dynamics. Second, the findings and CGM guidelines were derived under specific material and operational conditions. In applications involving cohesive powders, elongated/angular particles, or processes with high shear, moisture, or temperature variations, the optimal CGM factor may differ.

Furthermore, the influence of contact models and parameter settings on CGM responses was not addressed in this study. Since DEM simulations are inherently sensitive to contact force formulations, future investigations should perform systematic sensitivity analyses to evaluate how different model choices or parameter values may affect the reliability of CGM-based simulations. Therefore, further validation is necessary before extending our results to other material systems or industrial scenarios. Future work should consider the combined influence of particle shape and CGM scaling to evaluate the trade-offs between physical fidelity and computational efficiency more comprehensively.

In conclusion, CGM in DEM simulations offers a practical solution for achieving computational scalability without compromising the fidelity of mixing behavior analysis. The methodology and findings of this study are expected to serve as a reference for future industrial-scale DEM modeling, thereby facilitating the development of efficient, reliable, and cost-effective powder-mixing processes. Additionally, these insights may contribute to the advancement of simulation strategies applicable across diverse mixing-related industrial scenarios.

Author Contributions: Conceptualization and methodology, S.J.L. and S.-Y.H.; validation, formal analysis, investigation, data curation, S.J.L.; writing—original draft preparation, S.J.L. and S.-Y.H.; writing—review and editing, S.J.L. and S.-Y.H.; visualization, S.J.L. and S.-Y.H.; project administration and funding acquisition, S.-Y.H. All authors have read and agreed to the published version of the manuscript.

Funding: This work was supported by 2025 Ministry of Oceans and Fisheries (MOF) Marine Blue Tech Future Leader Training Project 'Training Blue Tech Leaders for Eco-Friendly Ships' (No. RS-2025-02220459).

Institutional Review Board Statement: Not applicable.

Informed Consent Statement: Not applicable.

Data Availability Statement: The raw data supporting the conclusions of this article will be made available by the authors on request.

Acknowledgments: This work was supported by the research grant (GNU-2024-240617) of the Gyeongsang National University in 2024.

Conflicts of Interest: Author Sung Je Lee was employed by the company TAE SUNG S&E. The remaining authors declare that the research was conducted in the absence of any commercial or financial relationships that could be construed as a potential conflict of interest.

Nomenclature

μ	friction coefficient
F_n	normal force
F_n^t	normal force in the HLS model
K_{nl}	contact loading stiffness
K_{nu}	contact unloading stiffness
S_n^t	normal overlap
γ	dimensionless constant
$K_{nl,p1}, K_{nl,p2}$	stiffness of the particle
L	particle size
E_p	bulk Young's modulus of the particles
ε	restitution coefficient
F_τ^t	tangential force in the LSCL model
S_τ	tangential overlap
K_τ	sliding stiffness
r_K	tangential stiffness ratio
f_{CGM}	CGM scale-up factor

L_{parcel}	diameter of scaled-up particle
L_{real}	diameter of original particle
m_{parcel}	mass of scaled-up particle
m_{real}	mass of real particle
k_{parcel}	stiffness of scaled-up particle
k_{real}	stiffness of real particle
$F_{contact,parcel}$	contact force of scaled-up particle
$F_{contact,real}$	contact force of real particle

Abbreviations

CGM	Coarse-grain modeling
DEM	Discrete-element method
HLS	Hysteretic linear spring
LMI	Lacey mixing index
LSCL	Linear spring Coulomb limit
RPM	Revolutions per minute

References

1. Bauer, W.; Nötzel, D.; Wenzel, V.; Nirschl, H. Influence of dry mixing and distribution of conductive additives in cathodes for lithium ion batteries. *J. Power Sources* **2015**, *288*, 359–367.
2. Thakur, R.K.; Vial, C.; Nigam, K.D.P.; Nauman, E.B.; Djelveh, G. Static mixers in the process industries—A review. *Chem. Eng. Res. Des.* **2003**, *81*, 787–826.
3. Badawy, S.I.; Lee, T.J.; Menning, M.M. Effect of drug substance particle size on the characteristics of granulation manufactured in a high-shear mixer. *AAPS PharmSciTech* **2000**, *1*, E33.
4. Hoornahad, H.; Koenders, E.A.B. Towards simulation of fresh granular-cement paste material behavior. *Adv. Mater. Res.* **2011**, 295–297, 2171–2177.
5. Chen, J.; Zeng, L.; Yin, J. Discrete element method (DEM) analyses of hot-mix asphalt (HMA) mixtures compaction and internal structure. *Adv. Mater. Res.* **2013**, 639–640, 1287–1294.
6. Remy, B.; Khinast, J.G.; Glasser, B.J. Discrete element simulation of free flowing grains in a four-bladed mixer. *AIChE J.* **2009**, *55*, 2035–2048.
7. Chandratilleke, G.R.; Yu, A.B.; Bridgwater, J. A DEM study of the mixing of particles induced by a flat blade. *Chem. Eng. Science* **2012**, *79*, 54–74.
8. Chandratilleke, G.R.; Yu, A.B.; Stewart, R.L.; Bridgwater, J. Effects of blade rake angle and gap on particle mixing in a cylindrical mixer. *Powder Technol.* **2009**, *193*, 303–311.
9. Siraj, M.S.; Radl, S.; Glasser, B.J.; Khinast, J.G. Effect of blade angle and particle size on powder mixing performance in a rectangular box. *Powder Technol.* **2011**, *211*, 100–113.
10. Chandratilleke, G.R.; Zhou, C.C.; Yu, A.B.; Bridgwater, J. Effect of blade speed on granular flow and mixing in a cylindrical mixer. *Ind. Eng. Chem. Res.* **2010**, *49*, 5467–5478.
11. Arndt, T.; Siegmann-Hegerfeld, T.; Fiedor, S.J.; Ottino, J.M.; Lueptow, R.M. Dynamics of granular band formation: Long-term behavior in slurries, parameter space, and tilted cylinders. *Phys. Rev. E* **2005**, *71*, 011306.
12. Fiedor, S.J.; Umbanhowar, P.; Ottino, J.M. Effects of fluid viscosity on band segregation dynamics in bidisperse granular slurries. *Phys. Rev. E* **2007**, *76*, 041302.
13. Huang, A.N.; Liu, L.C.; Kuo, H.P. The role of end wall shearing in the drum segregation band formation. *Powder Technol.* **2013**, *239*, 98–104.
14. Daumann, B.; Fath, A.; Anlauf, H.; Nirschl, H. Determination of the mixing time in a discontinuous powder mixer by using image analysis. *Chem. Eng. Sci.* **2009**, *64*, 2320–2331.
15. Cho, J.; Zhu, Y.; Lewkowicz, K.; Lee, S.; Bergman, T.; Chaudhuri, B. Solving granular segregation problems using a biaxial rotary mixer. *Chem. Eng. Process. Process Intensif.* **2012**, *57–58*, 42–50.
16. Williams, J.C.; Khan, M.I. The ixing and segregation of particulate solids of different particle size. *Chem. Eng.* **1973**, *269*, 19–25.
17. Shotton, E.; Orr, N.A. Studies on mixing cohesive powders. *J. Pharm. Pharmacol.* **1971**, *23*, 260.
18. Muzzio, F.J.; Robinson, P.; Wightman, C.; Dean, B. Sampling practices in powder blending. *Int. J. Pharm.* **1997**, *26*, 153–178.
19. Weidenbaum, S.S. Mixing of Solids. *Adv. Chem. Eng.* **1958**, *2*, 211–321.

20. Chou, S.-H.; Song, Y.-L.; Hsiau, S.-S. A study of the mixing index in solid particles. *KONA Powder Part. J.* **2017**, *34*, 275–281.
21. Huang, A.-N.; Kuo, H.-P. Developments in the tools for the investigation of mixing in particulate systems–A review. *Adv. Powder Technol.* **2014**, *25*, 163–173.
22. Lee, S.J.; Ahn, H.S.; Lee, J.H.; Kim, G.S.; Cho, J.H. Granule efficiency evaluation process using two-way CFD-DEM coupling analysis. *Chem. Eng. J.* **2024**, *498*, 155123.
23. Jiang, M.; Zhao, Y.; Liu, G.; Zheng, J. Enhancing mixing of particles by baffles in a rotating drum mixer. *Particuology* **2011**, *9*, 270–278.
24. Pereira, G.G.; Pucilowski, S.; Liffman, K.; Cleary, P.W. Streak patterns in binary granular media in a rotating drum. *Appl. Math. Model.* **2011**, *35*, 1638–1646.
25. Pereira, G.G.; Sinnott, M.D.; Cleary, P.W.; Liffman, K.; Metcalfe, G.; Šutalo, I.D. Insights from simulations into mechanisms for density segregation of granular mixtures in rotating cylinders. *Granul. Matter* **2011**, *13*, 53–74.
26. Ren, X.; Xu, J.; Qi, H.; Cui, L.; Ge, W.; Li, J. GPU-based discrete element simulation on a tote blender for performance improvement. *Powder Technolology* **2013**, *239*, 348–357.
27. Lemieux, M.; Léonard, G.; Doucet, J.; Leclaire, L.A.; Viens, F.; Chaouki, J.; Bertrand, F. Large-scale numerical investigation of solids mixing in a V-blender using the discrete element method. *Powder Technolology* **2008**, *181*, 205–216.
28. Kim, T.; Kang, B.; Jeon, M.; Chae, S. Recent progress and synthetic methods for single-crystalline cathode in lithium-ion batteries. *Ceramist* **2024**, *27*, 41–60.
29. Lacey, P.M.C. Developments in the theory of particle mixing. *J. Appl. Chem.* **1954**, *4*, 257–268.
30. Ansys Inc. *Ansys Rocky Theory Guide, Release 2024 R2*; Ansys Inc.: Canonsburg, PA, USA, 2024.
31. Ansys Inc. *Ansys Rocky CFD Coupling Guide, Release 2024 R2*; Ansys Inc.: Canonsburg, PA, USA, 2024.

Disclaimer/Publisher's Note: The statements, opinions and data contained in all publications are solely those of the individual author(s) and contributor(s) and not of MDPI and/or the editor(s). MDPI and/or the editor(s) disclaim responsibility for any injury to people or property resulting from any ideas, methods, instructions or products referred to in the content.